Precise measurement of the asymmetry parameter δ in muon decay

B. Balke,* G. Gidal, A. Jodidio,[†] K. A. Shinsky,[‡] H. M. Steiner, D. P. Stoker,[§]
M. Strovink, and R. D. Tripp
Lawrence Berkeley Laboratory and Department of Physics, University of California, Berkeley, California 94720

J. Carr**
Lawrence Berkeley Laboratory, University of California, Berkeley, California 94720
and Department of Physics, University of Colorado, Boulder, Colorado 80309

B. Gobbi
Department of Physics, Northwestern University, Evanston, Illinois 60201

C. J. Oram
TRIUMF, Vancouver, British Columbia, Canada V6T 2A3
(Received 9 June 1987)

Highly polarized μ^+ from the surface muon beam at TRIUMF have been analyzed by means of the muon-spin-rotation technique to determine the parity-violating muon decay asymmetry as a function of the daughter positron's momentum. The primary result is a determination of the muon decay parameter δ to high precision [δ=0.7486±0.0026(stat)±0.0028(sys)] consistent with the prediction δ=0.75 of the standard model of weak interactions. The implications of this measurement for generalized four-fermion contact interaction models of muon decay are discussed. The data are also used to constrain the parameters in certain left-right-symmetric and supersymmetric extensions of the standard model, and to limit the existence of lepton-number-violating scalar decays of the muon [$\mu \rightarrow e\sigma$, where $m(\sigma) < 80$ MeV/c^2].

I. INTRODUCTION

Since its formulation more than a decade ago, the standard $SU(2)_L \times U(1)$ model of the electroweak interactions[1] has been unfailingly upheld by experiment. Among the tests of the theory, muon decay has proven to be a very sensitive probe into the structure of the purely leptonic weak interactions, despite the fact that much of the decay information is carried away by the two final-state neutrinos. Specifically, in the most comprehensive generalization with massless neutrinos of the standard-model description of muon decay, only 10 combinations of the 19 possible parameters can be measured.[2] Determining the accessible parameters accurately is therefore critical if the generalized theory is to be constrained. The recent advent of highly polarized, high-flux "surface" muon beams has opened new possibilities, allowing high-precision measurements of the parameters which characterize parity violation. This potential has recently been exploited in a search for right-handed currents in muon decay, through a measurement of the degree of parity violation at the decay end point.[3] In the work reported here, the surface-muon technique is used in a precise measurement of the parity-violating decay asymmetry as a function of the positron momentum.

Our experiment improves on the last reported measurement of this type[4] with a twofold increase in both sample size and muon polarization, resulting in more than threefold improvement in the statistical sensitivity. However, as we sought to cover the same positron momentum range, the smaller momentum acceptance of our spectrometer required a wide range of field settings, heightening the potential for error in the determination of the positron momentum. Carrying out a demanding calibration procedure, we were able to equal the systematic sensitivity of Ref. 4. The combined uncertainties represent more than a factor of 2 improvement in precision over the prior measurement.

In terms of the general muon-decay theory, our asymmetry measurements are directly interpreted as a measurement of the decay parameter δ. These measurements are also used to set limits on certain extensions of the standard model, including supersymmetric theories with light sneutrinos and left-right-symmetric models with massive right-handed neutrinos. Lastly, the positron energy spectrum from unpolarized muon decay is searched for evidence of lepton-number-violating scalar decays, $\mu \rightarrow e\sigma$.

We begin with a discussion of muon decay and the muon-spin-rotation (μSR) experimental technique (Sec. II). Sections III and IV describe the apparatus and the event reconstruction. In Sec. V we discuss the momentum calibration. Section VI covers the asymmetry fits and corrections. The last two sections discuss the implications of the results; Sec. VII in terms of a measurement of δ, and Sec. VIII as concerns extensions of the standard model.

II. EXPERIMENTAL OVERVIEW

A. Muon decay

The experiment was designed to measure the parity-violating component of the stopped μ^+ decay rate as a function of the decay positron's momentum. The four-fermion[5] tree-level muon decay rate [Fig. 1(a)] is

$$\frac{d^2\Gamma}{dx \, d\cos\theta} \propto (x^2-x_0^2)^{1/2}\{6x(1-x)+\tfrac{4}{3}\rho(4x^2-3x-x_0^2)+6\eta x_0(1-x)$$

$$-\xi\cos\theta(x^2-x_0^2)^{1/2}[2(1-x)+\tfrac{4}{3}\delta(4x-3-m_e x_0/m_\mu)]\} , \tag{2.1}$$

where $\pi-\theta$ is the angle between the μ^+ spin direction and the outgoing e^+ momentum, $x=E_e/E_e(\text{max})$ is the reduced positron energy, $x_0=m_e/E_e(\text{max})$, and $E_e(\text{max})=(m_\mu^2+m_e^2)/2m_\mu=52.83$ MeV is the maximum positron energy. Parity violation is manifested in the term containing ξ, with δ parametrizing the momentum dependence. Since Eq. (2.1) integrates over all neutrino variables, sums over positron spins and factors out the overall decay rate, it exhibits only four of the ten measurable muon decay parameters.[2] Experimental[6] and standard-model $(V-A)$ values of these parameters are shown in Table I.
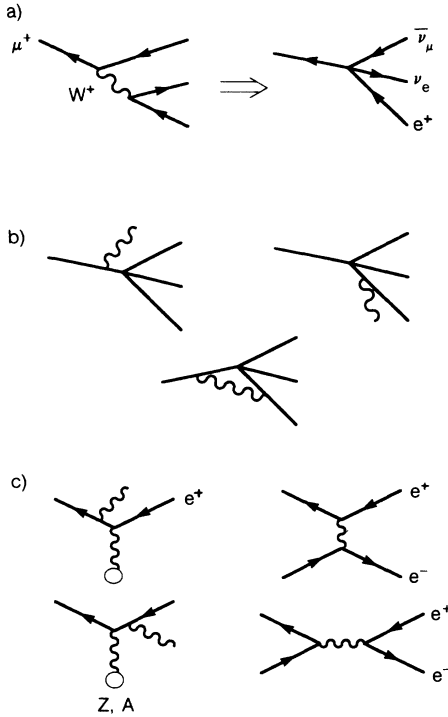
FIG. 1. Muon decay diagrams. Unless explicitly marked, all bosonic (wavy) lines are photons. (a) Tree-level Feynman diagrams for muon decay. The standard-model decay is on the left. In the limit $(m_\mu/M_W)\to 0$, we obtain the four-Fermi contact interaction diagram on the right. Equation (2.1) follows from the generalization of this diagram to all possible fermion couplings. (b) First-order QED internal radiative corrections to muon decay. (c) External radiative corrections: interactions of the final-state positron with the material of the apparatus. Bremsstrahlung is on the left, Bhabha scattering on the right.

Several modifications to Eq. (2.1) were made in our analysis. As shown in Fig. 2, internal radiative corrections[7] [Fig. 1(b)] have a percent-level effect on the decay rate. These corrections have been included in the analysis, although for brevity's sake not in Eq. (2.1) nor in subsequent equations. Similarly, bremsstrahlung[8,9] and Bhabha[8] interactions [Fig. 1(c)] of the positrons with material in the apparatus alter the reconstructed spectrum in the same sense, and by roughly the same magnitude, as the internal radiative corrections. These external radiative corrections are discussed in Sec. VI C and Appendix A. Next, in observing an ensemble we must average over the polarization of the initial-state muons. Then in Eq. (2.1) ξ becomes ξP_μ, where P_μ is the mean muon polarization along the chosen quantization axis, and $\pi-\theta$ becomes the angle between that axis and the outgoing positron direction. Lastly, in the equations below (though not in the analysis) we neglect m_e with respect to $E_e(\text{max})$ and m_μ. The decay rate is then

$$\frac{d^2\Gamma}{dx \, d\cos\theta} \propto x^2\{6(1-x)+\tfrac{4}{3}\rho(4x-3)$$

$$-\xi P_\mu \cos\theta[2(1-x)+\tfrac{4}{3}\delta(4x-3)]\} . \tag{2.2}$$

B. Experimental method

To maximize the experimental sensitivity to parity violation, we used highly polarized "surface" muons from the M13 channel at the TRIUMF cyclotron[10] (Fig. 3). Muons from pion decay at rest were transported through the highly symmetric channel and focused onto one of two aluminum stopping targets. Apart from

TABLE I. Muon-decay parameters. Standard-model $(V-A)$ theoretical values and experimental values of the parameters in Eq. (2.1). The measurement described here has not been included in the average for the value of δ.

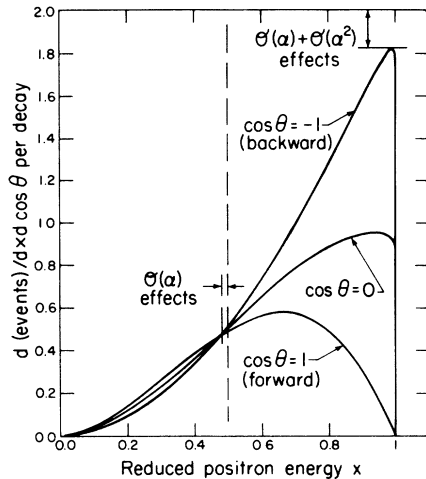|	$V-A$	Expt.
ρ	0.75	0.7517±0.0026
η	0	0.06 ±0.15
δ	0.75	0.7551±0.0085
ξP_μ	1	0.972 ±0.14
$\xi P_\mu \delta/\rho$	1	$0.9975 < \xi P_\mu \delta/\rho < 1(90\%$ C.L.$)$

FIG. 2. Muon decay spectrum. The standard-model differential muon decay rate in x and $\cos\theta$ vs the reduced positron energy x for $\cos\theta = +1$, -1, and 0 (unpolarized curve), where $\pi - \theta$ is the angle between the positron direction and the muon spin. Internal radiative corrections to first order are included throughout, second-order effects only near the decay end point at $x = 1.00$. The degree of parity violation is found from the difference between the forward and backward curves divided by twice the unpolarized curve.

FIG. 4. Experimental apparatus. $P1-P3$ and A are proportional chambers; $S1-S3$ are scintillators; $D1-D4$ are drift chambers. Veto scintillators $V1$ and $V2$ surrounding $S1$ and $S2$, respectively, are not shown. Muons were stopped in the target, and decay positrons were focused by the solenoid magnet into the spectrometer.

Coulomb scattering and possible small effects of right-handed currents, the incoming μ^+ spin direction was exactly opposite the μ^+ momentum direction. Two proportional chambers were used to measure the direction of motion. The muons passed through ≈ 60 mg/cm^2 of material before the target, and ≈ 111 mg/cm^2 within it before coming to rest. They were slightly depolarized after stopping through spin coupling with the magnetic moments of the aluminum nuclei.

As in a classic muon-spin-rotation experiment, the stopped muon spin was precessed and the decay rate measured as a function of time. Figure 4 shows the apparatus. Since the spin-precession field was applied per-
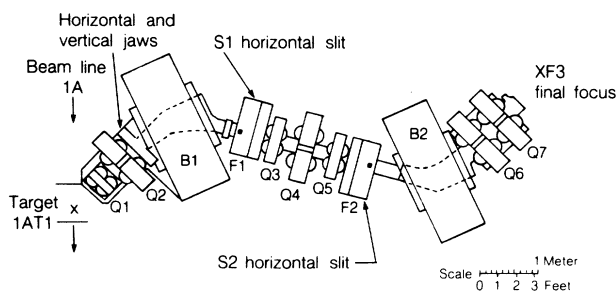

FIG. 3. $M13$ beam line. $B1$ and $B2$ are bending magnets, $Q1-Q7$ are quadrupole magnets. All magnets were thick lenses, the combinations $Q1-Q2$ and $Q6-Q7$ forming focusing doublets and $Q3-Q4-Q5$ forming a focusing triplet. $F1$, $F2$, and $F3$ indicate focal points of the source at 1AT1; $S1$, $S2$, and the jaws after $Q2$ were apertures. The magnification was -1 at the achromatic final focus $F3$, which coincides with the "Tgt" in Fig. 4.
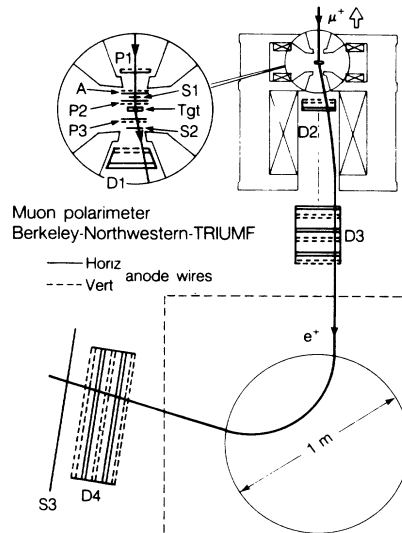
pendicular to the beam axis, the expected time dependence of the decay was an exponential with sinusoidal modulation [$\cos\theta \to \cos(\omega t + \theta_0)$ in Eq. (2.2)]. The ratio of the parity-violating and parity-conserving terms in Eq. (2.2) determined the magnitude of the modulation, and two different field strengths yielded either 9.6-MHz ("fast") or 5.9-MHz ("slow") precession frequencies. The muon spin direction at the instant of decay was known from the incoming muon direction, the precessing field strength, and the time interval between the arrival of the muon and the detection of the positron ("muon decay time").

Decay positrons were tracked and momentum-analyzed downstream of the target. To measure the positron direction at the decay point, the track was sampled by proportional and drift chambers as it traced an arc in a solenoidal magnetic field. Energy loss and straggling in ≈ 240 mg/cm^2 of material degraded the positron momentum before it was focused by the solenoid into the spectrometer. To reduce the effect of Coulomb scattering on the momentum resolution, the spectrometer volume itself was evacuated. Highly redundant track measurements at the spectrometer entrance and exit were used to determine the positron momentum. To cover the momentum range in $y = p_e / p_e(\text{max})$ from 0.36 to 1.00, the spectrometer acceptance of $\pm 20\%$ around the momentum setting Y_s required that six different values of the central field B_s be used: $B_s = B_{s,1}\Phi_s$, with $\Phi_s = 0.42$, 0.50, 0.60, 0.72, 0.86, or 1.00, and $B_{s,1} = 3186.7$ G. (Note: lower-case y denotes a particle momentum; Φ denotes the magnet field strength relative to a reference value; and capital Y, referred to as the magnet setting, denotes the characteristic momentum for particles transmitted at a given Φ.) The solenoid field

B. BALKE *et al.*

was scaled with the spectrometer field to maximize the total downstream angular acceptance.

Achieving a sensitive calibration of the spectrometer was critical, and required several sets of measurements. By varying the spectrometer setting Y_s to change the relative momentum of the end point of the muon decay spectrum, the sharp cutoff of the unpolarized spectrum at $y = 1.00$ was used to maximize the resolution of the momentum reconstruction. For the absolute calibration, the beam line was calibrated using the muon-decay end point and the decrease in muon flux in the beam line associated with the pion decay peak at $y = 0.5639$ (29.79 MeV/c in Fig. 5). With the assumption of linearity, these measurements determined the momentum Y_b delivered by the beam line as a function of the field strength in the bending magnets. Then, by varying Y_b with Y_s fixed, the spectrometer was calibrated using beam positrons. Corrections to the reconstructed momentum were formulated by comparing the reconstructed positron peak to the beam-line momentum setting. The experimental procedure was difficult, and the uncertainty in the calibration results contributed the largest systematic error to the determination of δ.

In addition to the μSR and calibration data, data were collected at all six spectrometer settings with a large (0.3-T) spin-holding field applied in the target region parallel to the beam axis. These "spin-held" data had an exponential muon-decay time spectrum unmodulated by muon spin rotation, and were used to set decay time cuts and to calibrate the muon-decay time clocks. Lastly, data were taken in many special runs to calibrate the wire-chamber positrons and to check stopping range and energy-loss calculations. A total of 3.0×10^7 spin-precessed triggers, 3.6×10^6 spin-held triggers, and 4.8×10^6 momentum calibration events were collected in a single three-week run. These data were written onto four hundred 1600 bytes per inch tapes. Analysis was carried out on the computer facilities at Lawrence Berkeley Laboratory, Northwestern University, and the University of Colorado at Boulder.
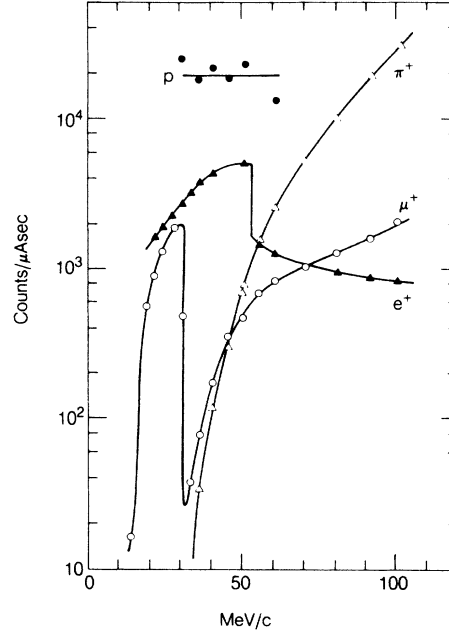

FIG. 5. M13 positive-particle flux. Flux in the M13 beam line at TRIUMF of different particle species vs beam-line momentum setting (adapted from Ref. 10). The data were collected with all slits and jaws in the beam line fully open. The dramatic decreases in muon flux at 29.79 MeV/c (highest momentum for muons from π^+ decay at rest in 1AT1) and positron flux at 52.83 MeV/c (highest momentum for e^+ from μ^+ decay at rest in 1AT1) were potential beam-line calibration points.

C. μSR analysis

Taking the initial (preprecession) axis of quantization to be opposite the incoming muon's direction, Eq. (2.2) implies the instantaneous spin-precessed decay rate,

$$\frac{d^4R}{dx\,dt\,d\Omega_e\,d\Omega_\mu} \propto e^{-t/\tau_\mu} A_e(x,\Omega_e)A_\mu(\Omega_\mu)x^2\{6(1-x)+\tfrac{4}{3}\rho(4x-3)-\xi P_\mu(t)\hat{\mathbf{p}}_e\overline{O}(\omega t)\hat{\mathbf{p}}_\mu[2(1-x)+\tfrac{4}{3}\delta(4x-3)]\} \ ,$$

where t is the interval after the muon arrival and τ_μ is the muon-decay lifetime; Ω_e and Ω_μ represent the positron and muon direction variables relative to the beam axis; $\hat{\mathbf{p}}_e$ and $\hat{\mathbf{p}}_\mu$ are the corresponding positron and muon unit direction vectors; A_e and A_μ are the positron and muon acceptance functions, normalized to unity at all x when integrated over the angular variables; $\overline{O}$ is a matrix describing the muon spin rotation; ω is the muon-spin-precession frequency; and P_μ is the muon polarization, including spin relaxation effects in the target. Integrating over angular variables:

$$\frac{d^2R}{dx\,dt} \propto e^{-t/\tau_\mu}x^2\left[6(1-x)+\tfrac{4}{3}\rho(4x-3)-\xi P_\mu[2(1-x)+\tfrac{4}{3}\delta(4x-3)]\int d\Omega_e\,A_e(x,\Omega_e)\hat{\mathbf{p}}_e\overline{O}(\omega t)\int d\Omega_\mu A_\mu(\Omega_\mu)\hat{\mathbf{p}}_\mu\right] \ .$$

$$(2.3)$$

For an isotropic decay, $A_e(x,\Omega_e)$ and its moments (such as the first integral above) can be determined from the measured distribution of decay particles. In a μSR experiment, such a sample is isolated by integrating the signal over a decay time interval $[t_1,t_2]$ such that

$$\int_{t_1}^{t_2} dt\, e^{-t/\tau_\mu}\overline{O}(\omega t)\int d\Omega_\mu A_\mu(\Omega_\mu)\hat{\mathbf{p}}_\mu \approx 0 \ . \qquad (2.4)$$

This requires that the average muon direction lies in the plane of the spin precession. If so, the anisotropic term

in Eq. (2.3) averages to zero, and in the large statistics limit:

$$\int d\Omega_e\, A_e(x,\Omega_e)\hat{\mathbf{p}}_e \approx \langle \hat{\mathbf{p}}_e(x)\rangle_{[t_1,t_2]} \ , \tag{2.5}$$

where the right-hand side is the average direction of the decay positrons detected in the interval $[t_1,t_2]$. Similarly, if the average positron direction is nearly in the plane of precession, for that same time interval,

$$\int d\Omega_\mu\, A_\mu(\Omega_\mu)\hat{\mathbf{p}}_\mu \approx \langle \hat{\mathbf{p}}_\mu\rangle_{[t_1,t_2]} \ . \tag{2.6}$$

For our apparatus both the muon and positron directions lay very nearly in the precession plane, and Eqs. (2.5) and (2.6) were excellent approximations.

As no absolute determination of the rate was made, the final fit was to the form [using Eqs. (2.5) and (2.6)]

$$\frac{d^2R}{dx\,dt} = N(x)e^{-t/\tau_\mu}\left[1 - M(x)\frac{P_\mu(t)}{P_\mu(0)}\langle \hat{\mathbf{p}}_e(x)\rangle_{[t_1,t_2]}\overline{O}(\omega t)\langle \hat{\mathbf{p}}_\mu\rangle_{[t_1,t_2]}\right] \ . \tag{2.7}$$

Here $N(x)$ is the spectrum normalization, and

$$M(x) = \xi P_\mu(0)\frac{2(1-x)+\tfrac{4}{3}\delta(4x-3)+\alpha h(x)}{6(1-x)+\tfrac{4}{3}\rho(4x-3)+\alpha g(x)} \tag{2.8}$$

is the muon decay asymmetry, with h and g describing radiative corrections.[7,8] As ρ is already well known,[6] measuring $M(x)$ primarily determines δ.

In principle, a precise measurement of the zero point x_z of the asymmetry, for which $M(x_z)=0$, would determine δ. At this point

$$\frac{d\delta}{dx}\bigg|_{x_z} = \frac{3}{2(4x_z-3)^2}\frac{1}{2} \ . \tag{2.9}$$

(The final factor of $\tfrac{1}{2}$ gives the reduction in sensitivity found empirically when fitting the data simultaneously for both δ and ξP_μ, as was necessary in this experiment.) As $x_z \approx 0.5$, one estimates that a determination of δ to ± 0.002 requires a precision approaching 0.002 in the momentum calibration at $x=0.5$. High precision in the momentum calibration near $x=1.00$ is implicit in this calculation, and held for our data.

We can also estimate the necessary precision in calculating the internal and external radiative corrections. For positrons which travel straight down the beam axis, Fig. 6 shows the motion of the zero point as the order-α radiative corrections are applied. For positrons moving through the solenoid with finite angle with respect to the axis, the effect of the external radiative corrections was less than that shown: Bhabha and bremsstrahlung energy loss caused a discontinuity in the track curvature, making the event susceptible to track quality cuts. In a detailed Monte Carlo simulation of the experiment, a 30% reduction in the effects of the external radiative corrections on $M(x)$ was found. Conservatively, then, Fig. 6 implies that an uncertainty of 10% in the radiative corrections can be allowed for a measurement of δ to 0.002. The order-α^2 QED internal radiative corrections to muon decay have not been completely calculated, but partial results[11] indicate that these will be at most 3–5 % of the order-α contributions. The uncertainty in the external radiative corrections[9] is also estimated to be 3–5 %. These are safely within the 10% limit.

III. APPARATUS

A. M13 beam line

As described above, the M13 beam line (Fig. 3) served both as a source of highly polarized muons and as a spectrometer for our momentum calibration. With regard to the first use, a detailed description can be found in Ref. 3. To summarize, muons were produced in the decay of π^+ generated by 500-MeV/c protons impinging on a 2-mm graphite production target at position 1AT1. The muons from pion decay at rest in the target were initially highly polarized. Those which were emitted from deep within the target, and were therefore likely to be depolarized through Coulomb scattering, were also likely to suffer substantial energy loss. They were effectively
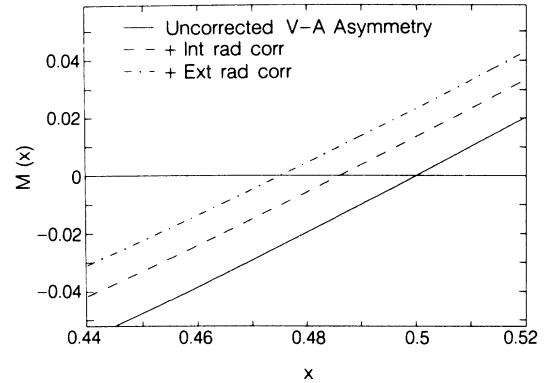

FIG. 6. Zero point of the decay asymmetry. The muon-decay asymmetry $M(x)$ vs the reduced positron energy x near its zero point at x_z [$M(x_z)=0$]. The "Uncorrected $V-A$ asymmetry" is the standard-model prediction without radiative corrections. The other curves indicate the effect on $M(x)$ of the radiative corrections of Figs. 1(b) and 1(c). In calculating the external radiative effects, the simplifying assumptions were made that positrons moved parallel to the solenoid field and that the event reconstruction and analysis had no biases against energy straggling. A realistic Monte Carlo simulation of the experiment reproduced only $\approx 70\%$ of the shift in x_z seen here due to external radiative corrections.

eliminated by the small momentum acceptance of the beam line, which was tuned for a 1% full width at half maximum (FWHM) momentum bite at 29.5 MeV/c. The remaining sample of muons was contaminated by $\approx 2\%$ of nearly unpolarized muons from pion decay in flight from the production target. The time correlation of these events with the short proton pulse (9 nsec, with a spacing of 43 nsec) facilitated their elimination by software "cloud muon" cuts. The final muon polarization was more than 99.6% (Ref. 3).

A thorough understanding of the beam line as a spectrometer was essential in obtaining a sound momentum calibration. The production target at position 1AT1 was viewed at 135° by the beam line (Fig. 3). Vertical and horizontal jaws just after $Q2$ defined the accepted solid angle. Positively charged particles (Fig. 5 shows the beam flux) were guided to a momentum-dispersed focus at $F1$ by the combined action of the quadrupole doublet $Q1-Q2$ and the bending magnet $B1$. The remainder of the beam line reversed the dispersion at $F1$ (for those particles accepted by the slit $S1$), producing a momentum-recombined focus at $F3$.

In principle, for a point source at 1AT1, every point along the momentum-selecting slit $S1$ at $F1$ would receive a different momentum, with a measured dispersion of 1.22 cm $/(\%\Delta p/p)$. In reality, the source had a finite size, which varied with the particle species, and each point in $S1$ received a finite range of momenta. With the rest of the beam line properly tuned, it was the combination of field strength in $B1$, position and width of $S1$, and source size which determined the momentum distribution of particles arriving at the final focus $F3$. With $S1$ and the beam spot fixed, the field strength alone determined the center of the transmitted momentum bite. For $S1$ width of 0.6 cm, typical of the momentum calibration data, Fig. 7 shows a sample positron spectrum (the curve is described in Appendix B).

Several chromatic effects were expected in the final particle distribution at $F3$, two of which were large enough to be readily apparent in the momentum calibration data. As the bend angle in $B1$ and $B2$ depended only on the horizontal projection of their momentum, particles with finite vertical slope in the bending magnets were biased toward larger momenta [Fig. 8(a); the coordinates are w along the beam axis, v vertical, and u horizontal, with $v'=dv/dw$, etc.]. Also, consistent with the smaller bend needed to reach $F3$ from $F2$, particles that appeared on the outside of the bend at $F3$ [negative u in Fig. 8(b)] had higher momentum than particles on the inside. This effect was also clearly seen. A surprise, though, was the cluster of events near $u=-1.2$ which were systematically low in y in comparison to the general trend of the distribution. We attribute this to the presence of approximately 250 mg/cm^2 of material upstream of $P2$ through which a small portion of the beam passed. The asymmetry in the muon-decay vertex distribution (Fig. 9) supports this conclusion: muons at low u were stopped before $P2$ by the extra material, and so did not activate the event trigger.

There were several systematic sources of deviation from ideal behavior in the beam line. First, the
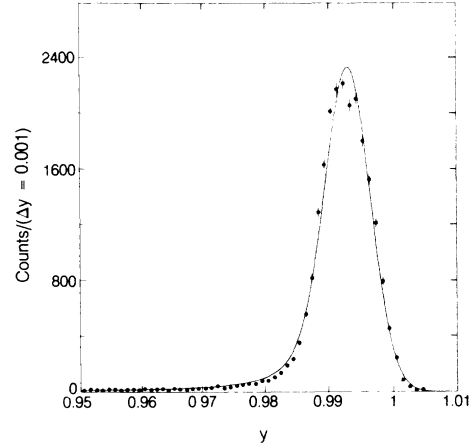

FIG. 7. Reconstructed beam momentum distribution. Measured beam positron spectrum in intervals $\Delta y=0.001$ vs the reduced positron momentum y. The long tail resulted from energy loss in 260 mg/cm^2 of material between the $M13$ vacuum window and the spectrometer. The curve is a fit of the data to a Gaussian with initial FWHM $\Delta y/y=0.6\%$, convoluted with the theoretical energy-loss spectrum and spectrometer resolution. For the data, the peak measures of Appendix B 1 are $y(\text{ave})=0.9928$ and $y(\text{fit})=0.9930$; for the curve $y(\text{ave})=0.9927$ and $y(\text{fit})=0.9933$.

computer-assisted beam-line monitor allowed the quadrupole current settings to be changed only in discrete steps of 0.5–1 % of the $Y=1.00$ setting. Second, the bending magnets induced a dipole component in their nearest-neighbor quadrupoles ($Q2$ and $Q6$). Finally, particle flux was usually maximized for off-center positioning of the slits $S2$, with weak dependence on the beam line setting Y_b. Particle trajectories were therefore not guaranteed to be symmetric about $Q4$. However, most importantly for the momentum calibration and the experiment as a whole, none of these effects would have affected the linear relation of the transmitted momentum to the field in the beam-line magnets, except possibly with the introduction of a zero-point offset.

Detecting and correcting instabilities in the beam line was also critical. Shifts in the position of the proton spot at 1AT1 by more than 1 mm were monitored by measuring the beam-halo current deposited on metal masks. Hall probes mounted on the pole faces were used to monitor the quadrupole settings. Finally, in the bending magnets $B1$ and $B2$, NMR probes and high-sensitivity Hall probes[12] were used to monitor to within 0.1% the scaling of the field integral (for "typical" particles) with the central field strength.

As summarized in Table II, a series of tests was made to verify that the momentum transmitted by the beam line was not strongly sensitive to variations in the beam-line parameters below the level at which they could be adjusted or monitored. In the upper half of the table, the beam-line momentum setting Y_b is seen to be relatively insensitive to the aperture parameters which determined the width and center of the positron momentum
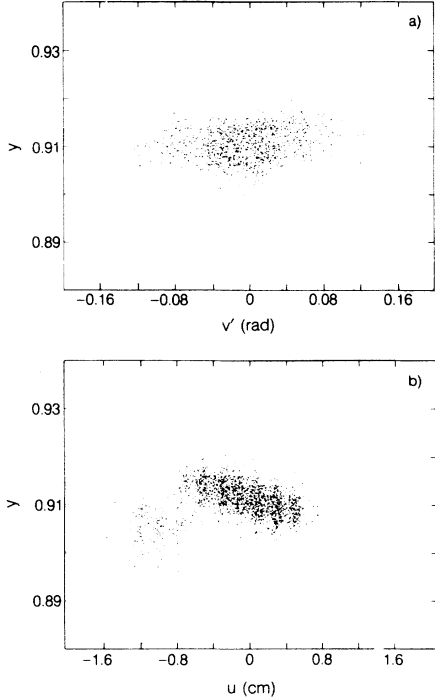
FIG. 8. Beam positron momentum correlations at $F3$. Correlations of the momentum delivered by the beam line with coordinates at the final focus $F3$, in a Cartesian system with w along the beam axis, u horizontal, v vertical, $u'=du/dw$, and $v'=dv/dw$. (a) Momentum y of beam positrons vs the vertical slope v' at $F3$. Cuts were made at $v'=\pm0.05$ rad. (b) Positron momentum vs the horizontal coordinate u at $F3$. (b) and Fig. 9 indicate the presence of unexpected material in the target area near $S1$. Cuts were made at $u=\pm0.7$ cm.

bite. By comparison, the systematic error for the data points used in the calibration was $\sigma_Y=0.0005$ (Sec. V and Appendix B). In the lower half of Table II we list the effect of changing the currents in the quadrupole magnets $Q1-Q7$ by one least count on the computer control system. These data enabled us to anticipate the
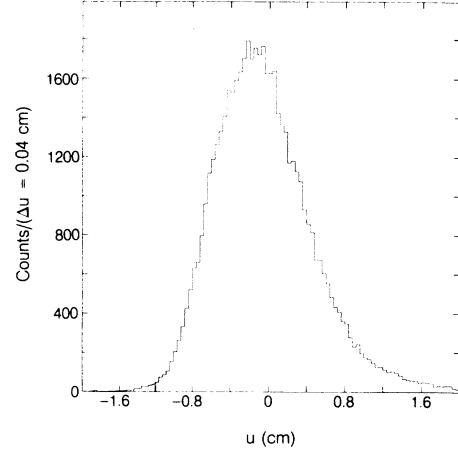

FIG. 9. Decay positron spot. See also the caption for Fig. 8. The distribution of decay positrons in intervals $\Delta u=0.004$ cm vs the horizontal coordinate u at $F3$. The deficiency in counts for $u<-0.8$ cm indicates that muons at low u were stopped before reaching the target by extra material near $S1$.

magnitude of the fluctuations in Y_b due to our inability to precisely adjust the magnet currents. Again, the effects seen are quite small. Finally, the shift in Y_b correlated with a change in the central field in $B2$ is given. Since the position of the beam positron spot at $F3$ was not the same at all Y_b, small adjustments in $B2$ (typically 0.05%) were necessary to center the spot at $F3$ during the calibration data taking. Although the cause of the instability in the positron spot was not determined, the overall conclusion was that the beam line was sufficiently stable to provide a calibration to 0.001 in y (Sec. II C, see also Appendix B).

B. Detector

The detector was triply segmented: the μ arm tracked and timed the arrival of particles from the beam line, and differentiated positrons from the heavier particles in

TABLE II. Correlation of beam-line parameters and transmitted momentum. Variation in the beam-line momentum setting Y_b with the beam-line parameters. "Least count" refers to the resolution of the digital beam-line control system when setting a given parameter. For the magnets the percentages are of the $Y_b=1.00$ current. For comparison the systematic error on the calibration data points was $\sigma_Y=0.0005$.

Parameter	Least count	$\Delta Y_b/Y_b$	ΔY_b
1AT1 proton spot moved	≈ 1 mm	<0.00024	
Horiz. jaw center	1 mm	-0.00002	
$SL1$ center	0.1 mm	-0.00005	
$SL1$, $SL2$ width	0.1, 0.1 mm	0.00000	
$SL2$ center	0.1 mm	0.00005	
$Q1$ current	0.5%		0.00002
$Q2$ current	0.8%		0.00012
$Q4$ current	0.5%		0.00002
$Q6$ current	1%		0.00013
$Q7$ current	0.8%		0.00017
$B2$	0.05%		0.0006

B. BALKE *et al.*

the beam; the *e* arm accurately measured positron tracks downstream of the target; the spectrometer measured the positron momentum. Considered in turn below, each segment consisted of a set of detectors built around a magnet. Reference should be made throughout to Fig. 4, the diagram of the apparatus. Further details may be found in Ref. 13.

1. μ arm

A low-mass design was required in the μ arm so that the low-energy muons would come to rest in the nondepolarizing aluminum stopping target, rather than in the detectors themselves. Proportional chambers $P1$ and $P2$ provided the tracking function, with 2-mm coordinate resolution (determined by the wire spacing) and 22-mrad angular resolution. Efficiencies for positrons were 90% in $P1$ and 95% in $P2$; and nearly 100% for the more heavily ionizing muons. Since the sensitive region of the counters was much larger than the expected beam spot, to eliminate beam halo a scintillation counter $V1$ (not shown in Fig. 4) was inserted just upstream of $S1$. Timing information was provided by scintillator $S1$ and proportional chamber A (identical to $P2$): the signal from $S1$ gated the muon-decay clock, and cathode signals from the A chamber were used (with 99.5% efficiency) to signal the presence of extra beam particles after the decay clock had been started.

Next, the beam particles entered an aluminum target. Two targets were used, with thicknesses of 151.0 and 181.0 mg/cm^2. With a calculated residual range for beam muons of 111.0 ± 6.9 mg/cm^2 into the aluminum[14] (the standard deviation is dominated by the statistical variation in the muon range[15]), these provided five and ten standard deviations of extra stopping power, but were thin enough to minimize the Bhabha and bremsstrahlung interactions of the decay positrons. The thicknesses were also such that the event trigger could cleanly differentiate beam muons and pions, which came to rest in the target, from beam positrons, which suffered less than $\Delta x = 0.01$ of energy loss. Most importantly the targets were nondepolarizing. Resting in the interstices of the aluminum lattice, the stopped muons coupled only in an average fashion with the spins of the nearby conduction electrons. As a result, the muon-electron spin-spin interactions which would have most rapidly depolarized the muons were almost completely absent. Residual muon depolarization due to coupling with the nuclear spins is briefly discussed in Secs. VI B and VII C.

The final component of the μ arm was the polarimeter magnet. Two sets of coils in the target region provided a longitudinal spin-holding field and a vertical spin-precessing field. The longitudinal field strength was 0.3 T, with transverse component less than 18 G (0.6%). The spin-precessing field, either 70 G ("slow" precession) or 110 G ("fast"), was measured to be uniform to better than 0.4%, with a longitudinal fringe component less than 1%. Shunt voltage readings at the power supplies were used to monitor the current in the magnets to 0.5%, ensuring field reproducibility throughout the course of the experiment. Furthermore, whenever the field was switched from the spin-holding to the spin-

precessing configuration, a longitudinal field of nearly 40 G remained in the target region. Using Hall probes of the concentrator type[12] as monitors, this field was zeroed to within 0.1 G by adjusting a small current passed through the longitudinal field coils.

2. e arm

The e-arm detectors, lying between the target and the end of the solenoid, served to track and time positrons from both muon decay and the beam line. The focusing properties of the solenoid magnet maximized the downstream acceptance, which was nearly 250 msr. In the design of the wire chambers, emphasis was placed on high spatial and angular accuracy in extrapolation back to the target. Proportional chamber $P3$ (identical to $P2$) provided a rough position measurement near the target, and its cathode signals were used in the event trigger. Drift chamber $D1$ was cone shaped with two vertical wire planes achieving 150-μm resolution, and two horizontal wire planes providing 800-μm resolution (the difference was not well understood). $D2$ was cylindrical, with two horizontal and two vertical planes all achieving 160-μm resolution. As in the μ arm, the e-arm chambers were very efficient: more than 95% of all tracks recorded at least nine of ten possible hits. The two scintillators $S2$ and $V2$ corresponded in function to $S1$ and $V1$ in the μ arm. $S2$ timed the positron signals, its output gating the drift-chamber electronics as well as stopping the muon decay clock. $V2$ vetoed off-axis positrons headed toward the magnet pole tips downstream of the target.

3. Spectrometer

The spectrometer drift chambers $D3$ and $D4$ provided high-precision track measurements for use in the momentum reconstruction. The chambers were mounted on the spectrometer vacuum box, each facing the magnet center at a radius of roughly 120 cm. The six horizontal and six vertical planes of $D3$ all had hit resolutions of 160 μm, while the wire planes in $D4$ (six vertical and four horizontal) all achieved resolutions of 250 μm. Both chambers were better than 97% efficient.

Behind $D4$ was a wall of three scintillators ($S3$) which provided a fast signal to the trigger logic to indicate that a positron had successfully traversed the spectrometer. Vertical segmentation and the timing difference between signals from left and right photomultipliers allowed a check on the track information registered in $D4$.

The spectrometer magnet was a cylindrically symmetric dipole with 37-inch-diameter pole faces and a 14.5-inch gap. At its highest setting the central field was 0.32 T. To monitor the field integral for typical tracks to within 0.1%, field measurements were made in the magnet midplane using an NMR probe in the central field and high-sensitivity Hall probes[12] at the central, 70% and 30% field points (Fig. 10).

The spectrometer was horizontally focusing. To minimize the effect of Coulomb scattering on the momentum reconstruction the Mylar vacuum box windows were positioned at the focal planes. The positron momentum
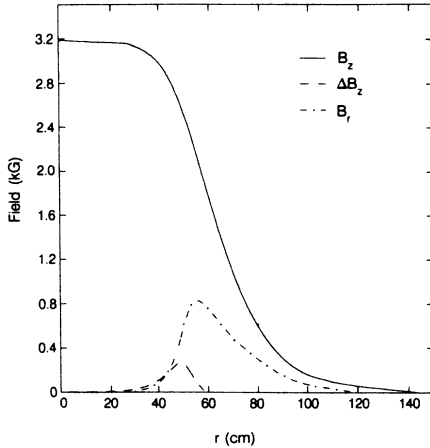
FIG. 10. Spectrometer field map. Strength in kG of the components of the spectrometer field vs radius r from the magnet center. z is the vertical coordinate in the cylindrical system with origin at the magnet center. B_z is the vertical field in the magnetic midplane, $\Delta B_z = B_z(z = 8) - B_z(z = 0)$ is the change in vertical field strength at $z = 8$ cm, B_r is the radial field strength at that same displacement from the midplane. The last two components varied with z as $\Delta B_z \propto z^2$, $B_r \propto z$.

FIG. 11. Trigger-logic diagram. Fast logic used to distinguish μ STOP, μ DECAY, and beam-positron straight-through ("ST THRU") events. The logic inputs are labeled by detector: the combined output of the A proportional chamber, the U and V planes of proportional chambers $P1$–$P3$, or the left-right (L or R) photomultiplier tube output for scintillators $S1$, $S2$, $V1$, and $V2$. The six G inputs represent the L-R output of the three vertical segments of scintillator $S3$. The Busy signal disabled the trigger while the online computer read the data registers and wrote an event to tape.

was then found to first order from the sum of the horizontal coordinates at the focal planes and the measured momentum dispersion 0.93 cm/($\%\Delta y/y$). However, this approximation broke down badly for particles which passed through the field far above or below the magnet midplane $z = 0$, as the large pole gap (40% of the magnet diameter) resulted in strong bowing of the field. In Fig. 10 we show the radial and vertical field "bumps" at $z = 8$ cm (positrons were accepted for the range $|z| < 16$ cm). By symmetry, it was expected that the strength of the radial component of the fringe field would behave as a polynomial in odd powers of z, and that intensification of the vertical field near the edges of the pole face would vary in even powers of z. We found empirically that it was sufficient to take $B_r \propto z$ and $\Delta B_z = B_z - B_z(z = 0) \propto z^2$. The field map was essential in the initial phase of the relative momentum reconstruction, which corrected for the largest part of the fringe-field-induced aberations (Sec. IV C).

IV. EVENT RECONSTRUCTION

A. The trigger

Three triggers were required in the experiment, distinguishing μ stops (momentum calibration), μ decays (main data sample), and beam positron "straight throughs" (momentum calibration and chamber alignment). The trigger elements (Fig. 11) were divided into two classes: "upstream" of the target ($P1$, $P2$, $S1$, and $V1$), and "downstream" ($P3$, $S2$, $V2$, and $S3$). The logic was built around two signals:

$$\text{BEAM} = P1 \cdot P2 \cdot S1 \cdot \overline{V1}$$

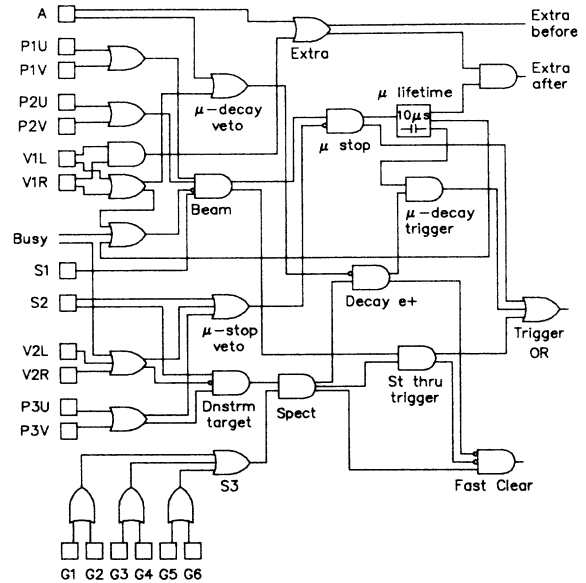indicated a fiducially allowed upstream track, while

$$\text{SPECT} = P3 \cdot S2 \cdot \overline{V2} \cdot S3$$

indicated a fiducially allowed downstream track. A beam straight through was recognized by the simultaneous signal

$$\text{ST THRU} = \text{BEAM} \cdot \text{SPECT} .$$

μ stops were identified as BEAM signals without any downstream activity:

$$\mu \text{ STOP} = \text{BEAM} \cdot \overline{P3} \cdot \overline{S2} \cdot \overline{V2} .$$

Each μ STOP trigger opened a 10-μsec gate, during which a SPECT signal without A or $V1$ activity (DECAY e^+ in Fig. 11) triggered a μ DECAY. The above event selection criteria reduced the rate of events written to tape to 35 Hz, or 0.1% of the beam flux.

The μ DECAY trigger had two major contaminants. The first, due to multiple muons in the stopping target, was mostly eliminated by an "extra before" flag, which tagged for later rejection events with BEAM signals up to 10 μsec before the μ STOP. The second background was from straight through positrons detected after a legitimate μ DECAY. These events were identified as "extra afters" by activity detected in the A, $P1$, or $P2$ counters during the remainder of the 10-μsec μ-decay gate, and later eliminated to avoid track reconstruction errors arising from the confusion of the two sets of drift-chamber hits. The effectiveness of these cuts is seen in Fig. 12, for worst-case data in which the spectrometer accep-
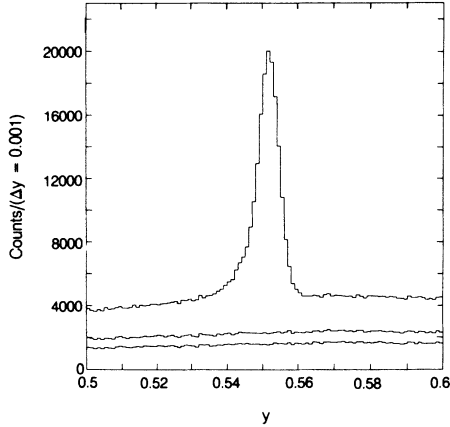
FIG. 12. Extra cuts: Spectrum of decay positrons in intervals $\Delta y = 0.001$ vs the reduced positron momentum y, showing contamination by beam positrons near $y = 0.55$ (upper curve). Applying "extra after" cuts (middle curve, Sec. IV A) eliminated the beam positron peak, isolating a pure μ-decay sample. The "extra before" cuts (lowest curve) rejected decays observed while multiple muons were in the target. The final sample was free of events composed of signals from unrelated muons and positrons.

tance overlapped the beam momentum ($y = 0.55$). The uncontaminated events which remained represented less than half the original sample.

B. Chamber calibration and track reconstruction

To the extent possible, chamber calibration was accomplished empirically. The drift-chamber space-time relationships were first estimated under the assumption that each cell was uniformly illuminated, and then fine-tuned by examining the residuals in the track fits.[13] Transverse alignment of the wire chambers was accomplished to within 50 μm using beam positrons collected with the solenoid field off.

For muon decay events, four track segments were reconstructed: the muon track in $P1$ and $P2$, the positron track in $P3$-$D2$ within the solenoid, and tracks in $D3$ and $D4$ at the spectrometer entrance and exit. Initially, all were fit to straight lines, with left-right ambiguities in the drift chamber hits resolved in the minimization of the residuals. After the first stage of the momentum reconstruction (Sec. IV C), the solenoid track was fit to a curve using transport matrices calculated in a first-order optics approximation to the solenoid field.[16] Occasionally the left-right ambiguities in $D1$ and $D2$ were resolved improperly in the initial straight-line fit. These errors propagated into the curved-track fit, inflating the curved track χ^2. However, the corresponding effect on the reconstructed positron target angles and position were shown in the Monte Carlo simulation to be negligible.

Many track-quality cuts were applied. Muon tracks were required to be unambiguous in all planes except one (of two) in $P2$, where the best hit could be chosen by comparison with the positron track. Ambiguous positron signatures were similarly rejected. χ^2 cuts, event

continuity checks, and aperture cuts were made on all fit tracks. None of these cuts eliminated more than a few percent of the events, as they were tuned to reject only genuine backgrounds (multiple tracks, scattered positrons, etc.), as opposed to events with small reconstruction inaccuracies. Lastly, the fringes of the muon and positron target angle distributions were conservatively cut to prevent contamination of the critical averages of Eqs. (2.5) and (2.6). Excluding events with $\cos\theta_\mu < 0.99$ and $\cos\theta_e < 0.975$ (θ is the angle with respect to the beam axis) reduced the sample by 30%. After all event quality cuts had been made, only 5% of the events written to tape remained for the asymmetry analysis of Sec. VI.

C. Relative momentum reconstruction

Prior to completing the absolute calibration of Sec. V B, our momentum reconstruction was limited to the determination of the positron momentum y in the spectrometer relative to the spectrometer setting Y_s. We therefore introduce the "relative positron momentum" $y_r = y / Y_s$. The determination of y_r had several increasingly accurate stages, starting in the first stage with an approximate model of the spectrometer optics. In this model, events at all field scaling factors Φ_s in the range $0.75 < y_r < 1.25$ were analyzed as though the spectrometer field were the $\Phi_s = 1.00$ field. The accuracy and resolution at this early stage were limited both by the nature of the algorithm and by the precision with which physical parameters such as the field map and the absolute positions of $D3$ and $D4$ were known. Even so, the method succeeded in providing a fairly accurate ordering of events by momentum at a given spectrometer setting. It was left to the calibration procedures described in Sec. V to fine-tune the relative momentum determination and to formulate the corrections which would enable a precise conversion of y_r to y.

The algorithm made an approximate reconstruction of the positron motion projected into the midplane of the spectrometer. The field was divided into three annuli separating the effects of its fringe, "bump," and central components (Figs. 10 and 13). Except for changes in slope at the fringe-"bump" interfaces, the vertical motion was taken to be constant. For the horizontal motion, the projected radius of curvature, calculated from the field integrals along the estimated particle path and the estimated y_r, was approximated as constant along each of the five track segments within the annuli, and infinite outside. The disagreement in the horizontal coordinate Δu between the extrapolated and measured tracks in $D4$ was then used to correct the estimate of y_r. Recalculating the radii of curvature, iterations were made until the final correction to y_r was less than 0.0005.

The approximate model reduced by a factor of 4 the 5–15 % fringe-field effects remaining after the first-order optics estimation of y_r (Sec. III B 3). Although the final resolution σ_y was a factor of 5 smaller than that achieved at this stage, the importance of this first step should not be underestimated. The μ-e edge studies (Sec. V A) used to formulate final corrections to the rela-
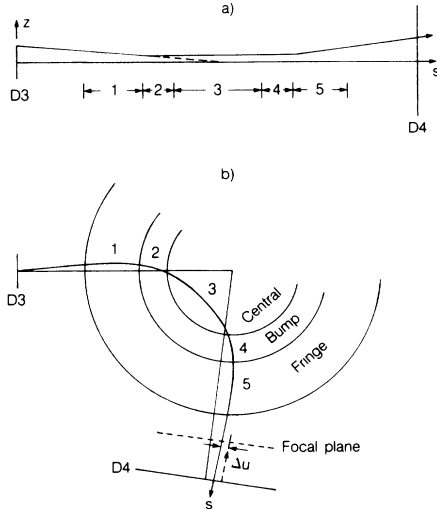
FIG. 13. Momentum reconstruction schematic. Simulated positron track from $D3$ to $D4$ through the spectrometer, illustrating one iteration of the reconstruction algorithm of Sec. IV C. The spectrometer field (Fig. 10) was divided into three regions (central, bump, and fringe) with boundaries at radii r of 36, 51, and 86 cm (circular arcs). (a) Vertical projection of the positron motion, showing the change in the vertical slope made at $r=51$ cm to simulate the effect of the radial component of the field. (b) The positron motion projected into the midplane of the spectrometer. The radius of curvature of the track was allowed to change only at the circular boundaries. The difference Δu between the forward (solid) and backward (dashed) extrapolations of the track at the exit focal plane was used to reestimate the momentum using the known spectrometer dispersion.

tive momentum were sensitive only to the high side of the momentum resolution function. While the effect of a symmetrical resolution in y on the asymmetry $M(x)$ is of order σ_y^2 at all x, an asymmetrical resolution has a lower-order effect. Our confidence that the finally corrected resolution is highly symmetrical is enhanced by the fact that this physically based initial momentum determination supplied most of the correction needed.

V. MOMENTUM CALIBRATION

To confidently combine the data collected at the six different spectrometer settings, an accurate momentum calibration was crucial. In planning the calibration procedure, three goals were identified. The first two were the determination to high resolution and high accuracy of the relative momentum $y_r = y/Y_s$ introduced in Sec. IV C. The third goal was an accurate calibration of the spectrometer setting Y_s as a function of the spectrometer central field strength. In attaining these goals, two sets of measurements were used. Examination of the reconstructed end point of the muon-decay spectrum enabled improvement in the resolution in y_r by a factor of 5 over that achieved with the model of Sec. IV C. Using the π-μ and μ-e decay reference points as momentum benchmarks and the highly linear beam line as a source, straight-through positrons were analyzed to determine

final corrections to the relative momentum scale and to calibrate the spectrometer.

We provide a brief dictionary of the notation used in the discussion that follows. Capital Y denotes a magnet setting and lower-case y denotes a particle momentum. All y are absolute ($y = 1$ at the muon-decay end point) except y_r, the relative momentum introduced in Sec. IV C. Φ denotes a central-field-scaling factor relative to $B_s = 3186.7$ G in the spectrometer magnet or $B_1 = 1555.4$ G in the first beam-line bending magnet. For the reference field strengths chosen, Φ and Y were approximately equal. Energy loss in the material of the apparatus, equal to momentum loss for the relativistic positrons, is indicated by Δx. The subscript b refers to the beam line while the subscript s refers to the spectrometer. The calibration points in π-μ or μ-e decay are indicated by subscripts $\pi\mu$ or μe.

A. Relative calibration

By varying the spectrometer central field, the $y = 1.00$ edge for spin-precessed data was swept through the spectrometer volume, simulating positrons of differing relative momentum y_r at a constant Φ_s. Nine samples of 1.2×10^5 events were collected, corresponding to relative momenta y_r between 0.84 and 1.17 (Table III). For each run, the values of y_r obtained from the initial determination discussed in Sec. IV C were plotted versus various track parameters (field integral, impact parameter b, and mean-squared deviation from the midplane $\langle z^2 \rangle$). Since the phase space of positrons accepted by the spectrometer varied slowly with y_r, up to a scaling factor the momentum distributions near the end point (Fig. 14) should have been the same for all values of a parameter. Whenever the edge distribution did show correlations with a parameter, a further *ad hoc* correction Δy_r was made to y_r as a function of that parameter to remove the correlations. For example, when the parameter was $\langle z^2 \rangle$, this correction took the form $\Delta y_r = f(y_r)\langle z^2 \rangle$

TABLE III. Spectrometer momentum resolution. Results of the relative calibration of Sec. V A using the end point of the muon decay spectrum (Fig. 14). Φ_s is the spectrometer field scale factor relative to $B_s = 3186.7$ G. $y_{r,\mu e} = 0.9917/\Phi_s$ is the expected relative momentum of the decay end point, y_r is the fit end-point momentum, and σ_y the fit resolution. The difference between the second and third columns is due to a combination of statistical fluctuations, spectrometer nonlinearity, and fringe-field effects.

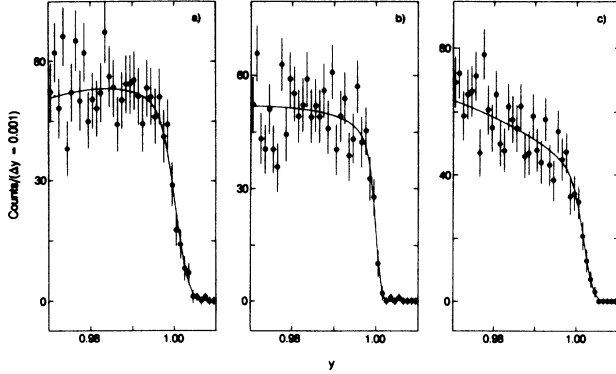| Φ_s	$y_{r,\mu e}$	y_r	σ_y
1.17	0.8476	0.8484(4)	0.0023(4)
1.13	0.8776	0.8779(2)	0.0021(2)
1.09	0.9098	0.9092(3)	0.0017(3)
1.05	0.9445	0.9440(2)	0.0011(3)
1.00	0.9917	0.9919(2)	0.0008(3)
0.95	1.0438	1.0445(3)	0.0011(4)
0.92	1.0779	1.0796(3)	0.0016(4)
0.88	1.1269	1.1282(4)	0.0020(3)
0.85	1.1666	1.1694(4)	0.0016(4)

FIG. 14. Momentum resolution fits. Decay positron spectrum in intervals $\Delta y = 0.001$ vs the reduced momentum y near the muon decay end point. The graphs (a)–(c) represent data taken with the spectrometer central field scaled from 3186.7 G by $\Phi_s = 1.17$, 1.00, and 0.85, respectively, correspond to fits one, five, and nine of Table III. The fit to the data, which extended to lower y than is shown, is described in Sec. V A.

where f is a polynomial of fourth order in y_r. Next, any correlations of y_r with the coordinates measured in chambers $D3$ and $D4$ were eliminated using the same procedure. The corrections were smallest ($< 1\%$) near $y_r = 1.00$, where the focusing action of the spectrometer was most effective. At low y_r, for which the fringe and bump irregularities had strongest effect, the corrections were larger, but still less than 4%.

Using data in a time range with zero average muon polarization (Eq. 2.4), the momentum resolution achieved was determined by fitting the reconstructed spectrum to the radiatively corrected, unpolarized standard-model spectrum smeared by a Gaussian resolution function. An offset of the end point from the expected position and corrections for the spectrometer acceptance were also included in the fit. The final resolutions, scaled by the spectrometer setting, are given in Table III. They ranged from about 0.1% to 0.2%. Representative fits are shown in Fig. 14, where a preliminary conversion from y_r to the initial positron momentum allows comparison of the reconstructed end points to $y = 1.00$.

B. Absolute calibration

The absolute calibration used the beam line as a source of known momentum positrons which, when passed through the spectrometer and analyzed using the relative calibration results, enabled us to determine the conversion from relative to absolute momentum (y_r to y). The central assumption of the absolute calibration was that the beam-line and spectrometer momentum settings (Y_b and Y_s) were linear in the magnet field strengths:

$$Y_b = m_b(B_1 - B_{1,0}) \,, \tag{5.1}$$

$$Y_s = m_s(B_s - B_{s,0}) \,. \tag{5.2}$$

Y_b is the mean of the momentum distribution (assumed

to be Gaussian) accepted by the beam line when the central field value in the first $M13$ bending magnet $B1$ is $B_1 = 1555.4\Phi_b$ G. Although we select B_1 in the discussion as a calibration standard, we note that the symmetry of the beam line made B_2 an equally good choice. Y_s is the factor which converts y_r to y when the central field in the spectrometer is $B_s = 3186.7\Phi_s$ G. Of the four parameters to be determined in the calibration, two were the conversion factors m_b and m_s. The beam-line zero-point offset $B_{1,0}$ was a correction for the effects of field hysteresis in the bending magnets and for offsets in the central field measurements; the spectrometer offset $B_{s,0}$ was a correction for those effects in the spectrometer, and for systematic shifts in the reconstructed momenta as well.

Under these assumptions we needed two reference points to calibrate the beam line, which could then be used as a momentum source to calibrate the spectrometer. In Fig. 5 two such benchmarks stand out: the decrease in muon flux at the π-μ decay edge ($p_{\pi\mu} = 29.79$ MeV/c or $y_{\pi\mu} = 0.5639$) and the decrease in positron flux at the μ-e end point at $y_{\mu e} = 1.00$ (52.83 MeV/c). Conveniently, these nearly span the range of momenta reconstructed in this experiment, $0.36 < y < 1.00$. The π-μ calibration (Fig. 15) is discussed in Sec. V B 1, the
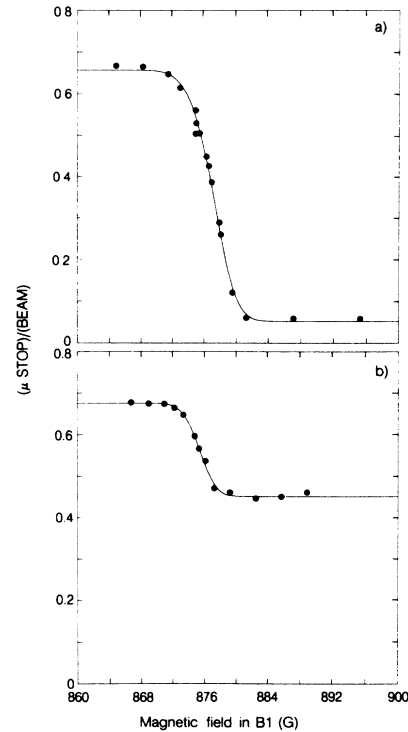
FIG. 15. π-μ calibration. See also the caption to Fig. 5. The fraction of the flux in $M13$ represented by muons [(μ STOP)/(BEAM)] as the central field strength in $B1$ was varied near the π-μ calibration point. Fitting these data found the beam-line momentum setting which centered the beam-line momentum acceptance at $Y_{\pi\mu} = 0.5639$. (a) and (b) show the earlier and later π-μ calibrations, respectively. The early measurement was made with 30 μA of primary proton current on 1AT1, the later with 130-μA current.

μ-e calibration in Sec. V B 2.

We completed the calibration with a procedure complementary to that of Sec. V A, passing beam positrons of varying momentum through the spectrometer at fixed Φ_s. This was done for each of the six values of Φ_s used for main data collection. The procedure and data reduction are described in detail in Appendix B.

The calibration information was combined in a global fit to determine the parameters of Eqs. (5.1) and (5.2) and the final corrections to the relative momentum of Sec. V A. Details of the fit are given in Appendix B. The fit results are illustrated in Fig. 16, which is used in Sec. V B 3 in estimating the uncertainties in the calibration.

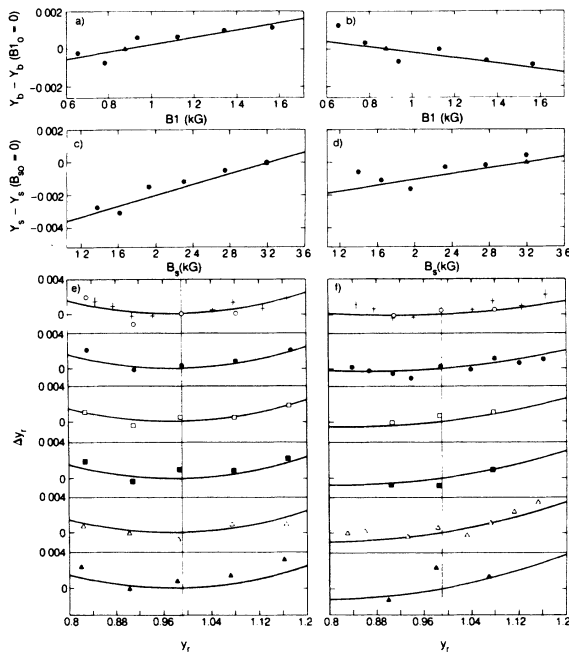FIG. 16. Momentum calibration results. See the text of Sec. V B 3 for a detailed discussion of the fit results and Appendix B for a description of the fit to the data points. On the left (right) are the results of the fit to the earlier (later) calibration data. The upper graphs (a) and (b) show the fitted corrections to the center Y_b of the momentum distribution transmitted by the beam line vs field strength in the bending magnet $B1$. The triangles are the π-μ calibration points (Fig. 15), and the circles correspond to the data points nearest the vertical line in the lower graphs (e) and (f). For the spectrometer calibration, (c) and (d) show the fitted corrections to the setting Y_s vs central field strength B_s in the spectrometer. The triangles near $B_s = 3200$ G are the μ-e calibration point; the data points are as in (a) and (b). For each of the six values of the field $B_s = 3186.7\Phi_s$ G ($\Phi_s \approx Y_s$), the lower graphs (e) and (f) show the final corrections Δy_r to the relative momentum y_r found by the reconstruction algorithm after applying the results of the relative calibration (Fig. 14, Sec. V A). The six sets of polygonal data points represent the beam positron calibration data taken with $\Phi_s = 1.00$ (open circles), 0.86 (filled circles), 0.72 (open squares), 0.60 (filled squares), 0.50 (open triangles), and 0.42 (filled triangles). The crosses at $\Phi_s = 1.00$ are the data in Table III from the decay end-point calibration of Sec. V A.

1. Beam-line π-μ calibration point

The π-μ calibration determined the bending magnet settings $(B_{1,\pi\mu}, B_{2,\pi\mu})$ which centered the beam acceptance at the pion decay momentum. This was done by sweeping the beam setting Y_b [Eq. (5.1)] across the momentum distribution of muons from π^+ decay at rest in the 2-mm carbon target at 1AT1 (Fig. 5). The δ-function muon momentum spectrum was smeared by energy loss inside the target, resembling near the end point a θ-function distribution falling off at $y_{\pi\mu} = 0.5639$. As Y_b was changed, the muon flux at $F3$ varied in proportion to the overlap of the muon spectrum with the beam-line momentum acceptance. Thus $B_{1,\pi\mu}$ was the field strength at which the muon flux was exactly midway between the muon fluxes measured when the acceptance fell completely inside or completely outside the θ function.

The detailed procedure was as follows. First, the beam line was carefully tuned near $Y_b = 0.5639$ by maximizing the muon flux and centering the muon spot at $F3$. Then B_1 was scanned from 864 G to 894 G in small steps while scaling the rest of the beam-line magnet fields in proportion to B_1. At each point we measured the ratio of rates

$$F = (\mu \text{ STOP})/(\text{BEAM})$$

$$\approx [R(\mu^+) + R(\pi^+)]/[R(\mu^+) + R(\pi^+) + R(e^+)] ,$$

where R is the flux of each beam particle species (Figs. 5 and 15). The flux of protons is not included in the expression because they stopped in the beam-line vacuum window before $P1$. The approximation depends on the chamber efficiency: a positron which did not register in the downstream chambers $P3$, $S2$, or $V2$ generated a μ STOP rather than a BEAM signal (Fig. 11). In Fig. 15(b), which shows data taken at high beam flux, evidence for such inefficiency can be seen in the excess of μ STOP's at high field strengths.

The measurement was made twice, at the beginning and midpoint of the experiment. The fit to the data shown in Fig. 15 is described in Appendix C. The results were $B_{1,\pi\mu} = 875.6$ G and $B_{2,\pi\mu} = 954.3$ G for the earlier and $B_{1,\pi\mu} = 874.8$ G and $B_{2,\pi\mu} = 952.6$ G for the later measurement. The statistical uncertainty in the fit values was estimated to be 0.2 G, much less than the difference between the two measurements. Possible reasons for the difference are considered in Appendix C, with the conclusion that one π-μ calibration cannot be preferred over the other. The results were therefore averaged, and the whole difference applied as a systematic error. As discussed in Appendix C, this was a conservative procedure.

2. Spectrometer μ-e calibration

The second absolute calibration point was obtained for the spectrometer using the μ-e edges in the data [Fig. 14(b)]. The beam-line calibration was then completed by analyzing beam positrons collected when Y_b was near 1.00, and comparing the reconstructed momentum with the edge position. In principle, the μ-e edge in the beam

line could have been used as the second beam-line calibration point, taking the ratio (BEAM)/(μ STOP) near $Y_b = 1.00$. Had this been possible, both m_b and $B_{1,0}$ in Eq. (5.1) could have been fixed. However, the rapidly rising heavy-particle flux, whose exact shape was not well known, undermined this measurement.

The most convenient way to make the μ-*e* calibration was to *choose* $Y_s = 1.00$ at $\Phi_s = 1.00$ [$B_s = 3186.7$ G in Eq. (5.2)], and to shift the reconstructed momentum scale of Sec. V A to put the μ-*e* end point at the proper value. Using the $\Phi_s = 1.00$ data taken intermittently throughout the course of the experiment, the decay edge was analyzed using the procedure described at the end of Sec. V A. Subtracting $\Delta x_s = 0.0083$ of energy loss upstream of the spectrometer vacuum box, the $y = 1.00$ decay end point was required to appear at $(y - \Delta x_s) = y_r = 0.9917$ on the reconstructed momentum scale. This condition was satisfied individually for each of the seven thin target runs analyzed with a reproducibility in y of 0.0002.

3. Calibration results

The final step of the calibration procedure, in which beam positrons were used to determine the final corrections to the momentum reconstruction, was performed twice, once early and once late in the experiment. Straight-through positron events were collected at each of the six spectrometer settings used in main data collection, with three to nine beam-line settings used to span the range in $Y_b/Y_s \approx y_r$ between 0.82 and 1.17. Each data point contributed three pieces of information to the calibration: the reconstructed position of the positron peak, the field strength in $B1$, and the field strength in the spectrometer. These data, with the edge scan results of Table III and the π-μ and μ-*e* calibration points, were input in a global fit to determine the four parameters in Eqs. (5.1) and (5.2) and a set of continuous curves which gave final corrections to the relative positron momentum y_r. Detailed descriptions of the data and fit are left to Appendix B. We concentrate here on estimating and understanding the systematic uncertainties of the calibration with a graphical comparison of the fits to the early and late data, shown side by side in Fig. 16.

After using the π-μ calibration point to eliminate m_b in Eq. (5.1), the calibration fit determined $B_{1,0}$ from the beam positron data. Figures 16(a) and 16(b) show the results of this beam-line calibration. The ordinate is the difference between the beam-line setting Y_b and the value expected from simple scaling from the π-μ calibration point (the triangle near 880 G). The line shows the effect of the fit value of $B_{1,0}$. The circles are the calibration data points in Figs. 16(e) and 16(f) nearest the vertical line at $y_r = 0.9917$. Since the corrections to y_r were constrained to be zero there, these data points determined the magnet zero-point offsets. The differences between the two curves was directly attributed to the difference between the two measurements of the π-μ calibration point.

Figures 16(c) and 16(d), which compare the spectrom-

eter setting calibrations for the early and late data, also reflect the π-μ calibration discrepancy. In this case, the μ-*e* calibration point was used to eliminate m_s from Eq. (5.2), leaving $B_{s,0}$ to be determined in the calibration fit. The ordinate is the difference between the spectrometer setting Y_s and the value expected from simple scaling from the μ-*e* point (the triangle near 3200 G). The data points are as in Figs. 16(a) and 16(b); the line shows the effect of the fit value of $B_{s,0}$. Comparing the early and late curves at $B_s = 1600$ G ($\Phi_s = 0.50$), we see that the uncertainty in the fit results was roughly 0.0010 near $Y_s = 0.50$. Equation (2.9) implies a corresponding uncertainty in δ of 0.0008.

Lastly, Figs. 16(e) and 16(f) show the correction Δy_r to the relative momentum y_r of Sec. V A. The results are plotted by spectrometer setting: $\Phi_s = 1.00$ uppermost (open circles representing the data points), followed by $\Phi_s = 0.86$ (filled circles), 0.72 (open squares), 0.60 (filled squares), 0.50 (open triangles), and 0.42 (filled triangles). The parabolic curves show the fit corrections, which were constrained to be zero at the vertical line ($y_r = 0.9917$). Plotted with the $\Phi_s = 1.00$ data are the edge scan data of Table III (crosses). Having been corrected for the fit value of $B_{s,0}$, these points compare directly to the curve.

The fit to the two sets of data gave quite different results. After scaling the differences by the spectrometer setting, the largest absolute disagreement is seen to be ≈ 0.0014 in y near $y_r = 0.84$ in the $\Phi_s = 1.00$ data. Our suspicion is that the discrepancy is due to a systematic downward shift in the later $\Phi_s = 0.86$ data, which was exacerbated by the lack of data far from $y_r = 0.9917$ at the other spectrometer settings. In this case the differences in the data should be reflected already in the determination of $B_{s,0}$. However, we conservatively accepted the differences between the curves as a systematic error in the calibration.

In establishing the final source of uncertainty in the calibration, we turn from Fig. 16 and recall that the symmetry of the beam line meant that the field strength in either $B1$ or $B2$ could have been used in Eq. (5.1). Although we chose $B1$ in the discussion, from a certain viewpoint $B2$ might actually have been preferred. For $B2$, the object at $F2$ and the image at $F3$ were both fixed, the latter by adjusting the current in $B2$ to position the positron spot on the target. In $B1$, only the image at $F1$ was fixed—the object source at 1AT1 was dependent on the particle species. This implied that the π-μ calibration of $B1$ using muons did not necessarily apply for positrons. However, considering the potential for asymmetries in the beam-line configuration (Sec. III A), that the positron spot at $F3$ was subjected to cuts not applied to muon events, and that the relative centering of the muon and positron spots at $F3$ was biased by material upstream of $P2$ which stopped muons but not positrons (Fig. 9), the same doubt was also cast on the π-μ calibration of $B2$. We used the difference between calibrations using B_1 and B_2 to estimate the importance of these effects.

In summary, there were eight possible ways of cali-

brating the spectrometer, choosing one of the combinations:

$$\{\text{early, late}\}\text{data}\times\{\text{early, late}\}\pi\text{-}\mu\times\{B_1,B_2\}\ .$$

The {early, late} differences accounted for uncertainty in determining the corrections to y_r and for calibration difficulties at the π-μ point; and the $\{B_1,B_2\}$ option accounted for possible differences in muon and positron behavior in the apparatus. Table IV summarizes the combinations used in Sec. VII to determine systematic errors by comparing calibrations between which only one of the options varied.

VI. ASYMMETRY FITS

Because the data were divided into distinct yet complementary samples, the asymmetry analysis required several steps. The main division in the data was between the spin-held and spin-precessed samples, with the latter further subdivided into four samples of (thin, thick) target × (fast, slow) precession. Finally, data in each class were collected at six different values of the spectrometer setting Y_s.

The analysis was organized to optimize the sensitivity with which the time-related parameters in Eq. (2.7) could be determined, thereby minimizing errors in the asymmetries. In the initial fits, data from all spectrometer settings were combined. The spin-held data calibrated the counting rate of the spin-precessed clock, while the combined spin-precessed data determined its offset relative to the muon arrival time. The combined thick and thin target data determined the polarization function $P_\mu(t)$ and the precession frequency ω for the fast and slow samples. With these quantities determined, the spin-precessed data were fit to find the decay asymmetries. As required by the dependence of the external radiative corrections on the target thickness and Y_s, in

these final fits the data were further subdivided by target type and spectrometer setting.

A. Spin-held data and fits

The spin-held data, which were critical for the decay clock calibration, are displayed in Fig. 17. Whenever the spectrometer setting was changed (see below), typically one or two runs of spin-held data were collected along with eight runs of spin-precessed data. After the first data-taking period (just before the later calibration), the μ-decay clock failed and was replaced. Cross calibration was performed by fitting a separate muon-decay lifetime τ_μ for each clock (Table V) using the exponential decay rate formula

$$R(t)=N_0\exp(-t/\tau_\mu)\ . \tag{6.1}$$

Then the second clock readout was scaled to make the lifetimes equal.

The spin-held data were also used to identify early time ranges during which "ringing" in the μ-arm proportional-chamber cables caused μ-stop events to self-veto the μ-decay trigger. The fit to Eq. (6.1) was repeated while varying the lower limit of the time range fitted. τ_μ decreased monotonically as times up to 1.4 μsec were excluded, after which it stabilized for the data in Fig. 17 at 2.200(8) μsec (the accepted value of the muon decay lifetime is $\tau_\mu=2.197$ μsec). Deviation at early times of the measured decay rate from an exponential is obvious. In the analysis of the spin-precessed data described below, only the time range from 1.4 to 8.8 μsec was fit.

TABLE IV. Calibration combinations. The calibration fits used in the analysis. E and L refer, respectively, to the early and later straight-through positron data sets and π-μ measurements. The results of the asymmetry fits for the six calibrations were averaged to obtain the final results, and the calibration errors were determined by taking differences between the calibration as indicated.

N_f	Data	π-μ	Magnet	Comment
1	E	E	$B1$	"Standard" earlier calibration
2	E	L	$B1$	$\pi\mu$ reproducibility (with 1)
3	E	E	$B2$	Beam μ^+-e^+ differences (with 1)
4	L	L	$B1$	"Standard" later calibration y_r correction reproducibility (with 2)
5	L	E	$B1$	$\pi\mu$ reproducibility (with 4) y_r correction reproducibility (with 1)
6	L	L	$B2$	Beam μ^+-e^+ differences (with 4)

FIG. 17. Spin-held decay rate. Time spectrum (counts in intervals $\Delta t=0.08$ μsec vs the muon decay time t in μsec) of the spin-held data collected with the first muon decay clock. The suppression at early times was due to self-vetoing of events soon after the muon arrival by ringing in the μ-arm proportional-chamber output. The unbiased time range ran from 1.4 to 8.8 μsec. The fit muon decay lifetime for data in this interval was $\tau_\mu=2.200(8)$ μsec; the accepted value is $\tau_\mu=2.197$ μsec.

B. Spin-precessed data and fits

The spin-precessed data were collected with cyclical variation of the spectrometer central field scaling Φ_s in the pattern $\Phi_s = 1.00$, 0.72, 0.50, 0.42, 0.60, 0.86, or the reverse. Two runs were taken at each setting for each of the combinations [{thin, thick} targets ×{fast, slow} precession] except at $\Phi_s = 1.00$, where only one run of each class was taken. Two different target thicknesses were used in order to check the effect of external radiative corrections. Two different precession frequencies were used to check the fit procedure, which required making precise time averages.

After all cuts described in Secs. IV B and V A were applied, the data were binned in x and t, and fit to Eq. (2.7)—appropriately averaged over the range of x and t in each bin—by minimizing the Poisson maximum-likelihood χ^2.[17]

Still to be clarified in Eq. (2.7) is the precise form of the polarization term $P_\mu(t)$. Selecting an appropriate form for the relaxation due to spin-spin coupling with the magnetic moments of the aluminum nuclei was problematic, as the data did not have the statistical power to differentiate between the two common forms: Gaussian and Kubo-Tomita "motional narrowing"[18] (the latter parametrizes a smooth variation between exponential and Gaussian forms for the relaxation). The situation was less favorable in this experiment than in the end-point analysis already reported, where a different trigger made it possible to use data at earlier decay times. As discussed below, we therefore chose to use the same depolarization fits obtained in Ref. 13. Still, it was impossible to choose between the Gaussian and Kubo-Tomita fits made there, which disagreed by nearly 1% in the extrapolation to $t = 0$. We (arbitrarily) selected the simpler Gaussian form of the spin relaxation in the fits described below:

$$P_\mu(t) = P_\mu(0)e^{-Gt^2} .$$

The implications of this choice are discussed in Sec. VII C.

Lastly, the clock offset relative to the muon stopping time ($t_{0,1}$ and $t_{0,2}$ for the first and second clock, respectively) had to be known to calculate both $P_\mu(t)$ and the precession phase ωt. With τ_μ, the parameters G, ω, $t_{0,1}$, and $t_{0,2}$ completely described the time dependence of the decay rate. A two-stage fitting procedure determined their values. In both stages, the fast and slow precession frequency data were fit separately, but the data for both targets and from all spectrometer settings were combined. For each of 16 bins in x covering the range $0.36 < x < 1.00$, events in the time range from 1.4 to 8.8 μsec were binned in 40-nsec intervals. In the first fitting stage, the data were split by the clock used. The fit parameters were G, ω, and t_0, and $N(x)$ and $M(x)$ for each of the 16 energy bins. In the second stage, with t_0 determined for each clock, the two samples were combined and fit by precession frequency for the final deter-

TABLE V. μSR time parameters. The fitted values of the parameters which described the time dependence of the spin-precessed decay spectrum. "First" and "Second" refer to muon decay clock in use when the data was taken. "Combined" refers to the total sample with the clock readouts brought into agreement using the fit values of τ_μ and t_0. F and S refer to fast and slow precession frequencies.

	First	Second	Combined
τ_μ (μsec)	2.200(8)	2.180(10)	
t_0,F	0.4484(10)	0.4357(7)	
,S (μsec)	0.4464(8)	0.4352(6)	
ω,F			9.571(3)
,S (μsec)$^{-1}$			5.929(2)
G,F			0.0029(3)
,S (μsec)$^{-2}$			0.0036(3)

mination of ω and G. The results for G, ω, and t_0 are given in Table V, and the combined data are plotted in Fig. 18.

As seen in Table V, the fit value of G disagreed by 1.6 standard deviations for data with slow and fast precession frequencies. To assess this possible discrepancy we
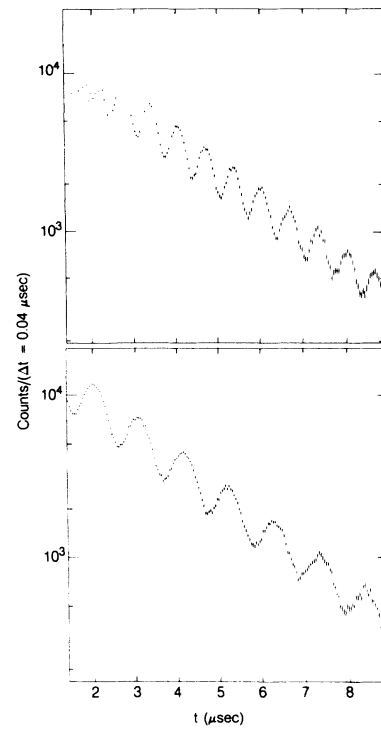

FIG. 18. μSR decay rate. Counts in intervals $\Delta t = 0.08$ μsec vs the muon decay time t in μsec for the μSR (spin-precessed) data. These combined fast (upper) and slow (lower) precession frequency data were used to determine the time constants which described the μSR signal. Only the time range fit is shown.

examined data from our previous μSR analysis[13] at the decay spectrum end point, for which the same two aluminum targets were used. As noted above, the polarization curve was better determined by those earlier data, which gave $G = 0.003\,78(20)$ μsec^{-2}. Since the difference between this single value of G and those in Table V did not significantly affect the fit values of ω and t_0, we used it in the fits described below.

For the final asymmetry fits, the correlation of cuts on the external radiative corrections (Secs. II C and VI C) with the spectrometer field strength Φ_s required that each spectrometer setting be fit separately. The energy ranges fit [Table VI(a)] were determined by the range over which the relative momentum calibration was performed; the bin size was fixed at 0.02 in x. The free parameters in the fit were only the normalization $N(x)$ and asymmetry $M(x)$ for each x bin. Of the parameters that were fixed, the uncertainties in ω, $t_{0,1}$, and $t_{0,2}$ did not significantly propagate into the fitted asymmetries, while the error in G had a smaller effect than exchanging the Gaussian for the motional narrowing form of the relaxation. Averaged over precession frequency and target type, the fit $M(x)$ are exhibited in Table VI(b), where the errors are statistical and do not reflect the uncertainty in G. Since the asymmetry corrections of Sec. VI C have been applied, the values are directly comparable to the theory with only internal radiative corrections.

The sensitivity of the data is demonstrated in Fig. 19, where data from different clocks and targets are combined to show the statistical power of the full sample. In the high-x data [Figs. 19(a) and 19(d)], the effect of spin-spin relaxation in suppressing the μSR signal at large decay times is clearly visible.

C. Monte Carlo simulation and asymmetry corrections

As mentioned in Sec. II C, a detailed Monte Carlo simulation of the experiment was required to calculate the asymmetry shifts due to external radiative corrections. When these corrections are included, the average asymmetry M_f expected at an energy x_f and spectrometer setting Y_s is given by

FIG. 19. Asymmetry fits. The μSR component of the muon decay rate in intervals $\Delta t = 0.08$ μsec vs the muon decay time t for fast- and slow-precession frequency data, illustrating the fit for the decay asymmetry $M(x)$. R(ani) is the parity-violating term (with ξ) in Eq. (2.3), R(iso) is the parity-conserving term. (a)–(c) are "fast" precession frequency data, (d)–(f) are "slow." The curves (a) and (d) show maximal parity violation in the energy range 0.96–1.00. The curves (b) and (e), including energies from $x = 0.44$–0.48, are near the zero point of the asymmetry. The asymmetry changes sign in the lowest-energy bin [(c) and (f), $x = 0.36$–0.40]. Only the time range fit is shown.

$$M_f(x_f, Y_s) = \frac{1}{N(x_f, Y_s)} \int d\Omega_e \int_{x_f}^1 dx_i \frac{d\Gamma(x_i)}{dx_i} M_i(x_i) \int d\epsilon \frac{dI(x_i, \epsilon)}{d\epsilon} \delta(x_f + \epsilon - x_i) A(\hat{\mathbf{p}}_e, x_i, \epsilon, Y_s)$$

$$\times \frac{\hat{\mathbf{p}}_e \cdot \langle \hat{\mathbf{p}}_\mu \rangle}{\langle \hat{\mathbf{p}}_e(x_f, Y_s) \rangle \cdot \langle \hat{\mathbf{p}}_\mu \rangle} , \tag{6.2}$$

with the spectrum normalization

$$N(x_f, Y_s) = \int d\Omega_e \int_{x_f}^1 dx_i \frac{d\Gamma(x_i)}{dx_i} \int d\epsilon \frac{dI(x_i, \epsilon)}{d\epsilon} \delta(x_f + \epsilon - x_i) A(\hat{\mathbf{p}}_e, x_i, \epsilon, Y_s) .$$
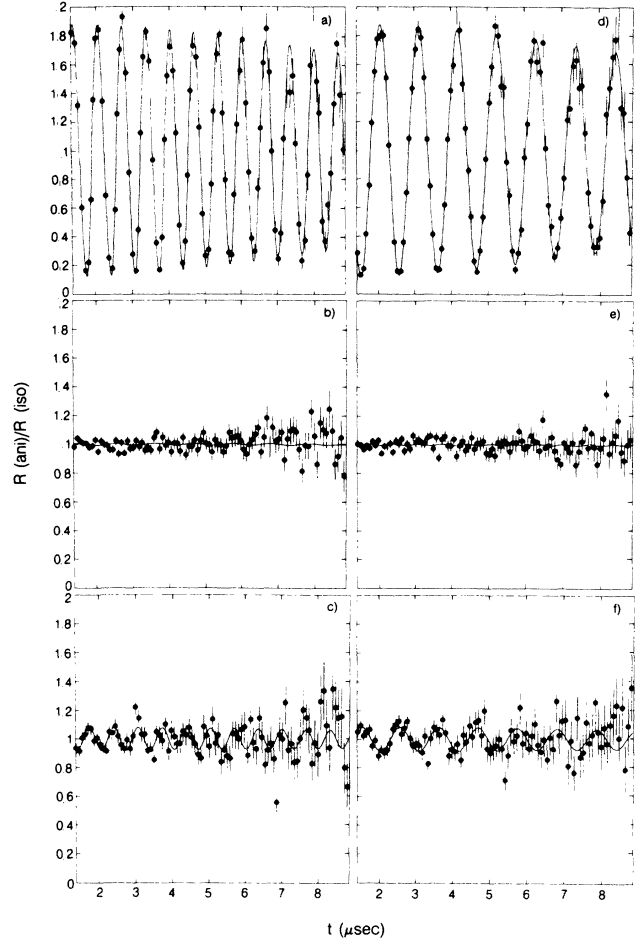
TABLE VI. (a) Asymmetry fits. The energy range and fit statistics for each of the four data sets. Φ_s indicates the spectrometer field strength; "thin" and "thick" refer to the two aluminum stopping targets; "fast" and "slow" refer to the muon spin-precession frequency. The events (Evts), χ^2, and degrees of freedom (DF) entries are in units of 10^3. The expected Poisson maximum-likelihood χ^2 is 2/DF. (b) Asymmetry fit results. The fit asymmetry $M(x)$ by spectrometer setting Φ_s for the calibration fit ($N_f = 5$) that was nearest the average of those in Table IV. Here we have averaged over precession frequency and target thickness. Since the effects of the external radiative corrections have been eliminated, the points are directly comparable to the theory with only internal radiative corrections. The errors σ_{cal} and σ_{rad} are the errors on $M(x)$ due to the uncertainties in the calibration results and the calculation of the radiative corrections to the decay spectrum. In the analysis of Sec. VIII C, these are used in setting limits on the parameters in extensions of the standard model.

(a)

| | | Thin | | | | Thick | | | | |
| | | Fast | | Slow | | Fast | | Slow | | |
Φ_s	x	Evts	χ^2	Evts	χ^2	Evts	χ^2	Evts	χ^2	DF
0.42	0.36–0.42	42	2.3	43	2.5	35	2.3	35	2.4	1.0
0.50	0.44–0.60	57	3.2	52	3.1	44	3.1	46	3.0	1.4
0.60	0.52–0.72	74	3.8	66	3.9	54	4.0	54	3.8	1.8
0.72	0.60–0.84	68	4.6	64	4.5	55	4.6	54	4.6	2.2
0.86	0.72–1.00	78	5.2	74	5.5	70	5.6	66	5.3	2.6
1.00	0.84–1.00	35	3.2	34	3.1	29	3.2	27	3.1	1.4

(b)

Φ_s	x	$M(x)$	σ_{cal}	σ_{rad}
0.42	0.37	−0.079(22)	0.0039	0.0014
	0.39	−0.084(10)	0.0039	0.0013
	0.41	−0.056(10)	0.0037	0.0012
	0.43	−0.033(8)	0.0035	0.0012
	0.45	−0.022(8)	0.0032	0.0011
	0.47	0.002(8)	0.0029	0.0011
0.50	0.45	−0.005(12)	0.0035	0.0010
	0.47	0.008(10)	0.0034	0.0010
	0.49	0.006(9)	0.0032	0.0010
	0.51	0.026(9)	0.0030	0.0010
	0.53	0.053(9)	0.0027	0.0010
	0.55	0.057(9)	0.0025	0.0010
	0.57	0.086(9)	0.0022	0.0010
	0.59	0.131(10)	0.0019	0.0009
0.60	0.53	0.060(12)	0.0031	0.0010
	0.55	0.070(11)	0.0029	0.0010
	0.57	0.099(10)	0.0027	0.0010
	0.59	0.117(9)	0.0025	0.0010
	0.61	0.127(9)	0.0023	0.0010
	0.63	0.170(8)	0.0021	0.0010
	0.65	0.187(8)	0.0019	0.0010
	0.67	0.223(9)	0.0017	0.0010
	0.69	0.242(9)	0.0015	0.0010
	0.71	0.274(10)	0.0012	0.0009
0.72	0.61	0.126(14)	0.0028	0.0010
	0.63	0.151(13)	0.0026	0.0010
	0.65	0.208(12)	0.0025	0.0010
	0.67	0.222(11)	0.0025	0.0009
	0.69	0.252(10)	0.0024	0.0009
	0.71	0.275(9)	0.0024	0.0009
	0.73	0.304(9)	0.0023	0.0009
	0.75	0.340(9)	0.0022	0.0008
	0.77	0.366(9)	0.0019	0.0008
	0.79	0.421(9)	0.0016	0.0008
	0.81	0.460(9)	0.0012	0.0008
	0.83	0.497(9)	0.0010	0.0007

TABLE VI. *(Continued).*

Φ_s	x	(b) $M(x)$	σ_{cal}	σ_{rad}
0.86	0.73	0.307(13)	0.0022	0.0009
	0.75	0.348(12)	0.0019	0.0009
	0.77	0.403(11)	0.0016	0.0009
	0.79	0.418(10)	0.0012	0.0008
	0.81	0.466(9)	0.0012	0.0008
	0.83	0.501(9)	0.0010	0.0008
	0.85	0.566(8)	0.0008	0.0007
	0.87	0.601(8)	0.0007	0.0007
	0.89	0.643(8)	0.0006	0.0007
	0.91	0.681(7)	0.0005	0.0006
	0.93	0.746(7)	0.0005	0.0005
	0.95	0.813(7)	0.0004	0.0004
	0.97	0.861(7)	0.0003	0.0004
	0.99	0.936(6)	0.0001	0.0001
1.00	0.85	0.535(13)	0.0015	0.0008
	0.87	0.596(11)	0.0012	0.0007
	0.89	0.630(11)	0.0009	0.0007
	0.91	0.697(9)	0.0006	0.0006
	0.93	0.746(9)	0.0004	0.0005
	0.95	0.814(8)	0.0003	0.0004
	0.97	0.869(7)	0.0002	0.0003
	0.99	0.955(6)	0.0001	0.0001

$d\Gamma/dx$ is the isotropic component of Eq. (2.1) and M_i is the asymmetry [Eq. (2.8)], both calculated for standard-model values of the decay parameters and including internal radiative corrections; $dI(x_i,\epsilon)/d\epsilon$ is the probability per interval $d\epsilon$ for the positron energy to change from x_i to $x_f = x_i - \epsilon$ due to bremsstrahlung and Bhabha scattering (Appendix A); A is the spectrometer acceptance, which depends on Y_s and the externally radiated energy loss ϵ; and the last factor accounts for the difference in angular distribution between straggled and unstraggled positrons. The averages of the unit momentum vectors are given by Eqs. (2.5) and (2.6).

Equation (6.2) was evaluated stochastically using a complete Monte Carlo simulation of the experiment for the thin-target data. Critical to the simulation were the inclusion of long tails in the smearing of hits in drift chambers $D1$ and $D2$ (to simulate occasional errors in resolving left-right ambiguities, Sec. IV B), and detailed calculation of positron interactions with the material of the apparatus between the target and the spectrometer vacuum, including Coulomb scattering, mean energy loss, Bhabha scattering, and bremsstrahlung. When calculating the external radiative corrections (Appendix A), the apparatus was decomposed by material along the particle path exactly as in the experiment. Each material was further decomposed into its constituent elements when evaluating $dI/d\epsilon$ in Eq. (6.2), and, for straggling in the target, corrections were included for the suppression of Bhabha events due to track ambiguity cuts in $P3$.

Although momentum analysis of Monte Carlo positrons was not necessary, they were propagated completely through the spectrometer field to allow the vertical apertures at $D4$ to have effect. The energy scales in the data and simulation were calibrated near $x = 1.00$ using the end-point fit of Sec. V A, and at lower energies with special Monte Carlo runs in which positrons were generated with fixed x.

The final Monte Carlo–event sample (4×10^5 events at each of the six spectrometer settings) was subjected to the standard analysis (except for track selection and momentum reconstruction). All cuts were applied, and in particular, a cut on the accuracy of the link between the tracks in $P3$-$D1$-$D2$ and $D3$ proved sensitive to extreme energy loss. Cuts on the χ^2 of the curved-track fit, which might also be expected to be sensitive to extreme energy loss, were instead ineffective because the above-mentioned left-right ambiguities completely dominated the residuals.

The asymmetry corrections were calculated for each x bin in the fit from the averages:

$$\langle M_i(x, Y_s) \rangle = \frac{1}{N_i} \sum_{\substack{\text{events at } Y_s \\ x - 0.01 < x_i < x + 0.01}} M_i(x_i) \, ,$$

$$\langle M_f(x, Y_s) \rangle = \frac{1}{N_f} \sum_{\substack{\text{events at } Y_s \\ x - 0.01 < x_f < x + 0.01}} M_i(x_f) \, . \tag{6.3}$$

Here N_i is the total number of events which were generated with energy x_i in the bin centered at x, and N_f is the number of events (after correcting for energy loss) which had final energy x_f in that same bin. The second average in Eq. (6.3) corresponds directly to Eq. (6.2). Since the event samples in corresponding initial and final energy bins were highly correlated, the difference $\Delta M = \langle M_i \rangle - \langle M_f \rangle$ between the two averages was statistically stable. We therefore added ΔM to the fit asymmetry M for each x bin to eliminate the effects of the external radiative corrections. The adjustment ranged from -0.0013 at $x = 0.99$ to -0.0115 at $x = 0.37$, with an estimated error varying over that range from 0.0002 to 0.0006.

Since energy loss in the target affected only the positron momentum without introducing any track discontinuities downstream, the thin-target simulation results could also be applied to the thick-target data, with corrections for the extra target material calculated analytically using Eq. (6.2) with $A = 1$ and $dI/d\epsilon$ for 30 mg/cm^2 of aluminum. The additional adjustments, ranging from $+0.0001$ to -0.0016, were applied when combining the thin- and thick-target data to yield the asymmetry values exhibited in Table VI(b).

VII. DETERMINATION OF DECAY PARAMETERS

After applying the corrections for Bhabha scattering and bremsstrahlung, the measured asymmetries [Table VI(b)] were used to determine δ and ξP_μ in a least-squares fit to Eq. (2.8). In evaluating the theoretical expression for $M(x)$ the decay parameter ρ was set provisionally to $\frac{3}{4}$ and $h(x)$ and $g(x)$ were evaluated from the expressions for the internal radiative corrections given in Ref. 7. The fit results are exhibited in Table
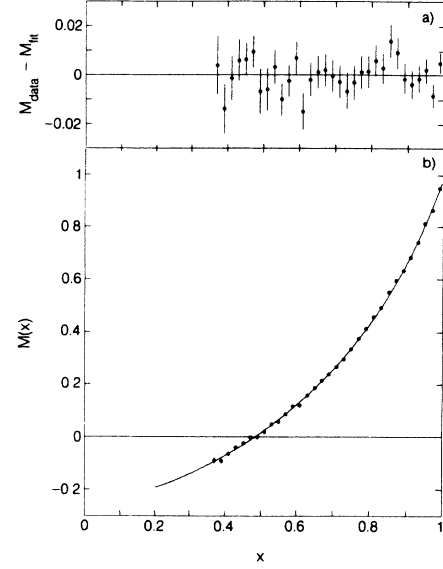

FIG. 20. Fit for muon decay parameters. The lower plot shows the fit muon decay asymmetry $M(x)$ vs the reduced positron energy x. The 32 data points represent the combined measurements of Table VI(b), and the curve is the fit to the theory with internal radiative corrections: Eq. (2.8) with the fit results $\delta = 0.7479$ and $\xi P_\mu = 0.9830$. The upper plot shows the statistical errors and fit residuals for the 32 data points.

VII and illustrated in Fig. 20. The average over the six calibration fits gave

$$\delta = 0.7479(26), \quad \xi P_\mu = 0.9830(35) , \qquad (7.1)$$

where the error is purely statistical. The individual results by target and precession frequency were entirely consistent. Since cloud muon cuts were not made (Sec.

TABLE VII. Decay parameter fits. The upper part of the table exhibits fit results for the muon decay parameters, with the data classified by target type and precession frequency. The Thick/Slow data contained a single point with X^2 of 25 whose removal did not affect the fit results. The lower half exhibits the fit results for the combined data for each of the six calibrations of Table IV. $N_f = 5$ corresponds to the combined upper half data [Table VI(b)].

Target	ω	δ	ξP_μ	X^2/DF
Thin	Fast	0.7491(51)	0.9734(67)	56/55
Thin	Slow	0.7481(50)	0.9866(67)	47/55
Thick	Fast	0.7562(56)	0.9763(75)	38/55
Thick	Slow	0.7370(54)	0.9954(72)	90/55

N_f	δ	ξP_μ	X^2/DF
1	0.7467(26)	0.9850(35)	240/229
2	0.7475	0.9837	
3	0.7473	0.9846	
4	0.7486	0.9815	
5	0.7477	0.9829	
6	0.7494	0.9804	
	0.7479(26)	0.9830(35)	

TABLE VIII. Decay parameters: systematic errors and corrections.

Source	$\Delta\delta \pm \sigma_\delta (\times 10^{-4})$	$\Delta\xi P_\mu \pm \sigma_{\xi P} (\times 10^{-4})$
Momentum calibration		
$\pi\mu$ reproducibility	± 9	± 14
μ-e differences	± 8	± 8
y_r corrections	± 11	± 22
Total	± 20	± 31
Momentum resolution	± 2	± 13
Radiative corr.	± 16	± 22
Energy-loss calculation	± 3	± 3
Muon scattering and contamination		8 ± 5
Total	0 ± 26	8 ± 41
World value ρ	7 ± 11	12 ± 17
Total	7 ± 28	20 ± 44

III A), the muon polarization was expected to be ≈ 0.98. Applying those cuts reduced the data sample by 25%, which then fit to

$$\delta^* = 0.7451(30), \quad \xi P_\mu^* = 0.9969(40) . \quad (7.2)$$

In making comparisons to the theory we used the high-statistics result δ and the high polarization result ξP_μ^*. These agree well with the standard weak interaction predictions for muon decay (Table I). The difference between δ and δ^*, a 1.6-standard-deviation effect for these two highly correlated samples, was assumed to be purely statistical in origin.

A. Systematic errors

We now discuss the systematic errors, summarized in Table VIII, in the determinations of δ and ξP_μ. As well as the physical effects described below, we checked for systematic effects in the asymmetry and decay parameter fits using a fake data generator. Excellent agreement with the input standard model values of δ and ξP_μ was obtained from the fits of the fake spectra.

1. Spectrometer calibration

The uncertainties in the spectrometer calibration manifested themselves independently in the spectrometer zero-point offset $B_{s,0}$ and in the curves which gave corrections to the relative momentum y_r. The two sources of error had their roots in (1) the beam-line π-μ calibration reproducibility (Sec. V B 1); (2) the uncertainty in the spectrometer μ-e calibration (Sec. V B 2); (3) the reproducibility of the magnet settings in the earlier and later calibrations (Sec. V B 3); and (4) muon-positron differences in the beam line (Sec. V B 3). Source 2 was negligible. In evaluating the others we took differences of the fits results in Table VII (as outlined in Table IV) to find the systematic errors in the calibration given in Table VIII. The errors from sources 1 and 4, which fed directly into the spectrometer zero-point offset, were added linearly. The error from source 3, which primarily affected the y_r correction curves, was then added in quadrature. The final calibration errors were $\sigma_\delta = 0.0020$ and $\sigma_{\xi P} = 0.0031$.

2. Momentum resolution

As mentioned in Sec. IV C the μ-decay edges used to fine-tune the momentum reconstruction were not sensitive to asymmetries in the resolution. Since all significant reconstruction asymmetries that we found were associated with events on the fringes of the track distributions within the spectrometer, such asymmetries could be detected as differences in the reconstructed μ-decay edge position in different parts of the positron phase space. Analyzing the edges in the thin target data with $\Phi_s = 1.00$ and 0.86 and in the edge scan runs described in Sec. V A we limited the existence of resolution asymmetries to levels corresponding to errors of $\sigma_\delta = 0.0002$ and $\sigma_{\xi P} = 0.0013$.

Since the calibration analysis was based on data taken with Φ_s near 1.00, the nonscaling of the spectrometer fringe field implied that the reconstruction was not necessarily accurate at lower Φ_s. Changing the shape of the spectrometer fringe field in the reconstruction algorithm of Sec. IV C by an amount which would reproduce the spectrometer zero-point effects at $\Phi_s = 0.42$, we reanalyzed the $y = 1.00$ data to find that the edge distributions remained the same. This implies that the nonscaling of the fringe field was not large enough to affect the momentum resolution.

3. Radiative corrections

There were three sources of uncertainty in the calculation of the radiative corrections. The single-most important source accounted for possible effects of higher-order QED diagrams on the internal and external radiative corrections to muon decay indicated in Fig. 1. As discussed in Sec. II C, the available estimates of the higher-order effects limit them to 3–5 % of the known corrections. Conservatively, we took the large number and assumed that the sign of the effect would be the same for both sets of corrections. Varying the corrections by 5%, we refit for the decay parameters to find the errors $\sigma_\delta = 0.0016$, $\sigma_{\xi P} = 0.0022$. Second, we made careful checks that the description of the apparatus and the sample size in the Monte Carlo simulation were sufficient for an accurate evaluation of Eq. (6.2). Finally,

the error in ΔM due to the assumption of standard-model values of the decay parameters in Eq. (6.2) was negligible.

4. Energy-loss and stopping-power calculations

Uncertainties in the calculation of the positron energy loss in the target and other material fed into the absolute momentum calibration. Analyzing the momentum distribution of straight-through positrons collected with and without extra material in the target region, we found 10% agreement between the observed changes in the peak position and the most probable energy loss Δ_{MP} calculated with the algorithms outlined in Appendix A. Theoretical and experimental comparisons in Ref. 19 also show this level of agreement. Fortunately, since the energy loss for beam and decay positrons was almost identical ($\Delta x = 0.0093$ and 0.0083, respectively), this uncertainty had only a small effect on the fitted values of the decay parameters ($\sigma_\delta = 0.0003$, $\sigma_{\xi P} = 0.0003$).

The muon stopping range was needed to calculate the residual range of the decay positrons in the target, and thus affected the energy loss and straggling calculations. From the calculations of Ref. 14, the range of 29.5-MeV/c muons in our apparatus was 171 mg/cm^2. Although there are few direct experimental checks of muon range calculations, experimental results for nonrelativistic protons show 1% agreement with theory. Since the energy-loss mechanisms for low-energy muons and protons are identical, this implies a 2-mg/cm^2 uncertainty in the muon range. The corresponding effect on the positron energy loss and straggling calculations was negligible.

B. Corrections

The final significant systematic error in the determination of δ and ξP_μ arose from the uncertainty in the world-average value of the decay parameter ρ, currently known to be 0.752 ± 0.003.[6] Using this value in Eq. (2.8) and refitting for the decay parameters gave the shifts $\Delta\delta = +0.0007 \pm 0.0011$, $\Delta\xi P_\mu = +0.0012 \pm 0.0017$.

Track-reconstruction errors affected the calculation of the acceptance-weighted averages of $\langle \hat{\mathbf{p}}_\mu \rangle$ and $\langle \hat{\mathbf{p}}_e \rangle$ in Eqs. (2.5) and (2.6). Chamber alignment errors, finite hit resolution, the curved track-reconstruction approximations, and Coulomb scattering all contributed. The results exhibited in Eqs. (7.1) and (7.2) include corrections for these effects, determined in the Monte Carlo simulation, of $\Delta\delta = 0.0000$ and $\Delta\xi P_\mu = +0.0004$. The errors in these corrections were estimated to be less than 0.0002.

Lastly, we included a correction to ξP_μ for all calculable sources of muon depolarization (this excludes the spin relaxation discussed in the next section). Using the analysis of Ref. 13, we multiplied ξP_μ by 1.0008 ± 0.0005. We did not include the additional correction factor of 1.0007, calculated in Sec. 4.2 of Ref. 13, for depolarization due to μ-e scattering. That calculation was based in part on Eq. (21) of Ref. 20, which turns out not to be correct:[21] the factor m_e/m_μ should instead be $2m_e/E$. The actual depolarization due to μ-e scattering is negligible.

C. Final results

As discussed in Sec. VI B the form of the muon spin-relaxation curve $P_\mu(t)$ was a delicate point in the analysis. In fact, there is no complete theoretical analysis of spin-spin relaxation in room-temperature metals.[22] Furthermore, the relaxation observed in our targets is greater than that which has been seen in other measurements of muon spin relaxation in aluminum.[23] Possibly this is from the imperfections of the crystal lattice introduced during the cold-rolling manufacturing process. Our experimental situation was thus even further removed from the regular-lattice models considered theoretically. To determine whether the theoretical uncertainty was critical, the two available forms of the relaxation (motional narrowing and Gaussian) were used separately in the μSR fits of Sec. VI B. Subsequent fits for the decay parameters showed a 1% difference in ξP_μ in the two cases.

Because of this serious uncertainty, we choose only to quote a result for δ, which was insensitive to the form of the relaxation. Combining the systematic errors enumerated in Table VIII, the analysis with $\rho = 0.75$ gives

$$\delta = 0.7479 \pm 0.0026 \pm 0.0026 \ .$$

Using instead the world-average value of ρ,

$$\delta = 0.7486 \pm 0.0026 \pm 0.0028 \ .$$

The final result is in excellent agreement with the standard model of weak interactions (Table I).

VIII. IMPLICATIONS

A. Muon-decay analysis

The primary implications drawn from muon decay measurements are limits on the coupling constants of the generalized effective four-Fermion contact interaction. Several equivalent parametrizations of the theory exist.[2,24] Currently the most popular is the helicity-

TABLE IX. Limits on couplings in generalized μ-decay theories 90%-C.L. limits on the contributions of the couplings $g^i_{\alpha\beta}$ to the muon decay Hamiltonian and the muon decay rate (final column). i is the Lorentz structure of the coupling, α and β, respectively, indicate the handedness of the electron and muon, n and m, respectively, the handedness of the electron and muon neutrinos (Sec. VIII A).

i	$\alpha\beta$	nm	$\|g^i_{\alpha\beta}\|$ ($\times 10^{-3}$)	BR
S	RR	LL	< 66	$< 0.1\%$
S	LR	RL	< 125	$< 0.25\%$
S	RL	LR	< 424	$< 2.5\%$
S	LL	RR	< 918	$< 20\%$
T	RL	LR	< 122	$< 4\%$
T	LR	RL	< 36	$< 0.4\%$
V	RR	RR	< 33	$< 0.1\%$
V	LR	LR	< 60	$< 0.25\%$
V	RL	RL	< 110	$< 1\%$
V	LL	LL	> 888	$> 79\%$

projection form of Ref. 24, in which the Hamiltonian is written (μ^- decay)

$$H = \frac{G_0}{\sqrt{2}} \sum_{i=S,V,T} \sum_{\alpha,\beta=R,L} g^i_{\alpha\beta} \, \bar{e}_\alpha O^i \nu_{en} \bar{\nu}_{\mu m} O^i \mu_\beta + \text{H.c.}$$

Here α and β are the handedness of the electron and muon; i labels the interaction type, with $O^S = 1$, $O^V = \gamma^\mu$, and $O^T = \sigma^{\mu\nu}$ the possible Lorentz-covariant couplings in the Dirac theory of spin-$\frac{1}{2}$ particles; n and m, the handedness of the electron and muon neutrinos, follow from α, β, and i (Table IX); the $g^i_{\alpha\beta}$ are complex coupling constants. Since $g^T_{LL} = g^T_{RR} = 0$, there are only ten complex parameters, representing 20 real parameters less one arbitrary phase, to be constrained by experiment. The standard-model theory has the particularly simple parametrization $g^i_{\alpha\beta} = 0$, except $g^V_{LL} = 1$. For small deviations from the standard model, δ is given by

$$\delta \approx \tfrac{3}{4}[1 + Q_{LR} - Q_{RL} - 4(B_{LR} - B_{RL})] ,$$

$$Q_{RL(LR)} = \tfrac{1}{4} |g^S_{RL(LR)}|^2 + |g^V_{RL(LR)}|^2 + 3 |g^T_{RL(LR)}|^2 ,$$

$$B_{RL(LR)} = \tfrac{1}{16} |g^S_{RL(LR)} + 6g^T_{RL(LR)}|^2 + |g^V_{RL(LR)}|^2 .$$

The recent experimental efforts of the SIN Collaboration in measuring the electron polarization[25] and our earlier measurement of $\xi P_\mu \delta/\rho$ (Ref. 3) have yielded significant improvement in the precision of the constraints on the $g^i_{\alpha\beta}$ (Refs. 26 and 27). Substituting the final result reported here for our preliminary result $\delta = 0.748 \pm 0.005$ (Ref. 28), an analysis of the type carried out in Refs. 26 and 27 yields essentially the same limits as those reported by Stoker.[27] The final experimental status is summarized in Table IX. The branching-ratio limits there were calculated from the normalization condition on the total lifetime:

$$\sum_{\alpha,\beta=L,R} (\tfrac{1}{4} |g^S_{\alpha\beta}|^2 + |g^V_{\alpha\beta}|^2) + 3(|g^T_{RL}|^2 + |g^T_{LR}|^2) = 1 .$$

B. Extensions of the standard model

Gauge-theoretical extensions of the standard model which have recently attracted attention include left-right- (L-R-) symmetric[29] and supersymmetric[30] models. In many variations of these models, no effect on muon decay is expected because the unobserved particles in the final state (ν_R or $\tilde{\nu}$, in the L-R and supersymmetric models, respectively) are expected to have masses much larger than the muon mass. Thus the masses of the virtual intermediates in the decay (W_R and $\tilde{W}$) can be constrained by muon decay only in cases in which the final-state particles are less massive than the muon.[31]

In L-R-symmetric models,[29] the electroweak gauge group is expanded to $SU(2)_R \times SU(2)_L \times U(1)_Y$. Parity is unbroken at high energies. At low energies, in the absence of W_L-W_R mixing, the difference in the W_L and W_R masses [$m(W_L)$ and $m(W_R)$, respectively] reduces the contributions of the right-handed sector by a factor $\epsilon_R = [m(W_L)/m(W_R)]^4$. When $m(W_R) \gg m(W_L)$, the theory is then consistent with observed low-energy phe-
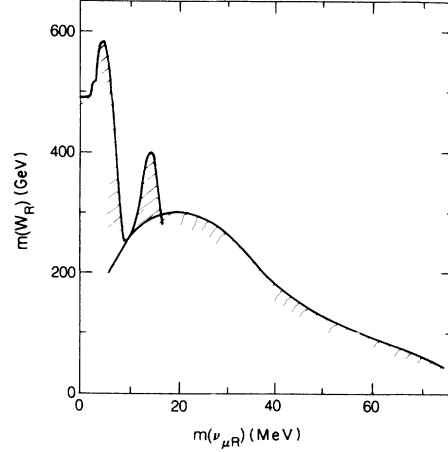

FIG. 21. W_R mass limits. 90%-C.L. limits on the mass of a hypothetical gauge boson W_R vs the right-handed muon neutrino mass $m(\nu_{\mu R})$ in left-right-symmetric extensions of the standard model of weak interactions. The area below the curves is disallowed. The strong limits shown as peaks near $m(\nu_{\mu R}) = 0$ are from the analysis of Ref. 3.

nomenology. In muon decay the effect of the right-handed sector is to decrease the parity violation illustrated in Fig. 2. In the simplest L-R models, δ remains exactly $\frac{3}{4}$. To escape this result, one or both of the right-handed neutrinos in the final state must have a non-negligible mass. If $m(\nu_{eR}) + m(\nu_{\mu R}) < m_\mu$, the shape of the asymmetry spectrum is altered because the end points of the left- and right-handed decays do not coincide. Alternatively, if decay via the W_R is forbidden because one or both of the right-handed neutrinos are extremely heavy, mixing between the left and right neutrino families would still allow right-handed contributions to the decay, with $\delta = \frac{3}{4}$ (Ref. 32).

In Fig. 21 we present limits for the first scenario in the particular case $m(\nu_{eR}) = 0$. We obtain 90%-C.L. limits on the W_R mass (assuming no mixing with W_L) vs $m(\nu_{\mu R})$. The strong limits near $m(\nu_{\mu R}) = 0$ were obtained from our previous end-point rate analysis.[3] The data reported here extend the limit to $m(W_R) > 160$ GeV/c^2 at $m(\nu_{\mu R}) = 50$ MeV/c^2. Details of the analysis are given in Sec. VIII C.

In supersymmetric theories, each standard-model particle gains a partner, denoted with a tilde, which is identical to the original except for a difference in intrinsic spin of one-half unit. In these models, the muon can decay via W-ino exchange into an electron and two sneutrinos ($\tilde{\nu}$). The decay spectrum has been analyzed by Buchmüller and Scheck.[33] With $m(\tilde{\nu}_e) = 0$, they use the experimental values of ξ, δ, and ρ to constrain $m(\tilde{W})$ vs $m(\tilde{\nu}_\mu)$. In the case $m(\tilde{\nu}_\mu) = 0$, they find

$$\rho = \frac{3}{4}\left[1 + \frac{\epsilon_S}{2 + 3\epsilon_S}\right], \quad \delta = \frac{3}{4}\left[1 - \frac{3\epsilon_S}{2 + 3\epsilon_S}\right],$$

$$\xi = 1 + \frac{4\epsilon_S}{2 + 3\epsilon_S}, \quad \epsilon_S = \frac{m(W)^4}{m(\tilde{W})^4} .$$

The experimental values of ρ and δ combine to give the most sensitive limits. The result for δ reported here extends the 90% confidence limit from $m(\tilde{W}) > 240$ GeV/c^2 to $m(\tilde{W}) > 280$ GeV/c^2.

For $m(\tilde{\nu}_\mu)$ finite, we obtain limits by comparing the theoretical asymmetry spectrum (standard model and supersymmetry combined) to our measured asymmetries. Figure 22 shows the 90% C.L. on $m(\tilde{W})$ from this analysis. Without the input of ρ the limit shown at $m(\tilde{\nu}_\mu) = 0$ is weaker than the one stated above. However, in the range of $m(\tilde{\nu}_\mu)$ shown in Fig. 22, our results are still much stronger than those from the best collider searches. For example, the limit from the ASP Collaboration[34] is indicated by the straight line in Fig. 21. They obtain $m(\tilde{W}) > 61$ GeV/c^2 for $m(\tilde{\nu}) = 0$, and limits of that magnitude out to $m(\tilde{\nu}) = 10$ GeV/c^2.

$$\frac{d^2\Gamma_R}{dx\, d\cos\theta} \propto \theta(1 - r_R - x)\epsilon_R E^2 \left[3 - 2x + r_R \frac{3-x}{1-x} - \cos\theta \left[1 - 2x - r_R \frac{1+x}{1-x} \right] \right] ,$$

$$E = 1 - \frac{r_R}{1-x}, \quad \epsilon_R = \frac{m(W_L)^4}{m(W_R)^4}, \quad r_R = \frac{m(\nu_{\mu R})^2}{m_\mu^2} .$$

The theta function $\theta(t)$ is 0 for $t < 0$, and 1 for $t \geq 0$. We have normalized the decay spectrum with Eq. (2.1), so the isotropic and anisotropic components of the combined spectrum can be seen to be

$$R_R(\text{iso}) = 3 - 2x + \alpha h(x)$$
$$+ \theta(1 - r_R - x)\epsilon_R E^2 \left[3 - 2x + r_R \frac{3-x}{1-x} \right] ,$$

(8.1)

$$R_R(\text{ani}) = 1 - 2x + \alpha g(x)$$
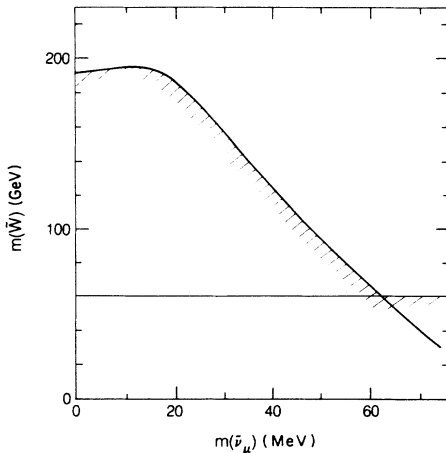$$- \theta(1 - r_R - x)\epsilon_R E^2 \left[1 - 2x - r_R \frac{1+x}{1-x} \right] .$$

FIG. 22. W-ino mass limits. 90%-C.L. limits on the mass of the $\tilde{W}$ vs the mass $m(\tilde{\nu}_\mu)$ of the muon sneutrino in supersymmetric extensions of the standard model of weak interactions. The area below the curves is disallowed. The horizontal line at $m(\tilde{W}) = 61$ GeV represents the limits of Ref. 34.

Details of the analysis used to obtain the limits on the mass of the $\tilde{W}$ are given in the next section.

C. Constraints on extensions of the standard model

In general, there are three unknown masses in these theories: the masses of the two undetected particles in the final state (n_e and n_μ, where n is either ν_R or $\tilde{\nu}$), and the mass of the gauge particle (Ω, which is either W_R or $\tilde{W}$). To simplify the analysis we set $M(n_e) = 0$. This leaves two parameters in the theory: $\epsilon = [m(W_L)/m(\Omega)]^4$ and $r = [m(n_\mu)/m_\mu]^2$.

1. L-R-symmetric model

Shrock has calculated the muon decay spectrum for massive neutrinos.[35] Adapting his results for a $V + A$ decay with $m(\nu_{eR}) = 0$, we have

$h(x)$ and $g(x)$ represent only the internal radiative corrections. The asymmetry is then found to be [cf. Eq. (2.8)]

$$M_{\text{new}}(x) = P_\mu \frac{R(\text{ani})}{R(\text{iso})} ,$$

(8.2)

which was compared to the measured asymmetries [Table VI(b)] to obtain the mass limits.

2. Supersymmetric models

Buchmüller and Scheck[33] have calculated the W-ino-mediated muon decay spectrum:

$$\frac{d^2\Gamma_S}{dx\, d\cos\theta} \propto \theta(1 - r_S - x)\epsilon_S E^3 [3 - x + \cos\theta(1+x)] ,$$

$$E = 1 - \frac{r_S}{1-x}, \quad \epsilon_S = \frac{m(W_L)^4}{m(\tilde{W})^4}, \quad r_S = \frac{m(\tilde{\nu}_\mu)^2}{m_\mu^2} .$$

Corresponding to Eq. (8.1) we have

$$R_S(\text{iso}) = 3 - 2x + \alpha h(x) + \theta(1 - r_S - x)\epsilon_S E^3(3-x) ,$$

(8.3)

$$R_S(\text{ani}) = 1 - 2x + \alpha g(x) - \theta(1 - r_S - x)\epsilon_S E^3(1+x) .$$

We used these expressions in Eq. (8.2) and compared to the data, as described next, to set the mass limits.

3. Description of the fit

After averaging over the targets and precession frequencies, we had 58 data points for comparison with Eq. (8.2). For a given value of r we mapped out the χ^2 distribution as a function of ϵ for $m(\Omega)$ between $m(W_L)/2$ and infinity (P_μ was for each value of ϵ to obtain the minimum χ^2). Converting from χ^2 to probability assuming a normal χ^2 distribution, we calculated the 90%-confidence limits on ϵ, and thus the gauge mass. The

unphysical region $\epsilon < 0$ was excluded in the calculation of the limits. In performing the fit, the 58×58 error matrix for the asymmetries was calculated from the expression:

$$E_{ij} = \delta_{ij}\sigma^2_{i,\text{stat}} + \sigma_{i,\text{cal}}\sigma_{j,\text{cal}} + \sigma_{i,\text{rad}}\sigma_{j,\text{rad}} \, ,$$

using the uncertainties presented in Table VI(b).

D. Rare decays

Family extensions of the axion solution to the strong CP problem have been suggested which predict the decay $\mu \rightarrow e\sigma$, where σ is a pseudoscalar.[36] Such a decay would appear as a narrow peak in our positron energy spectrum, with a width dominated by the spectrometer resolution. In searching for such peaks we obtain limits on the branching ratio $\Gamma(\mu \rightarrow e\sigma)/\Gamma(\mu \rightarrow e\nu\nu)$. Our data were sensitive for masses $m_\sigma < 80$ MeV and life-
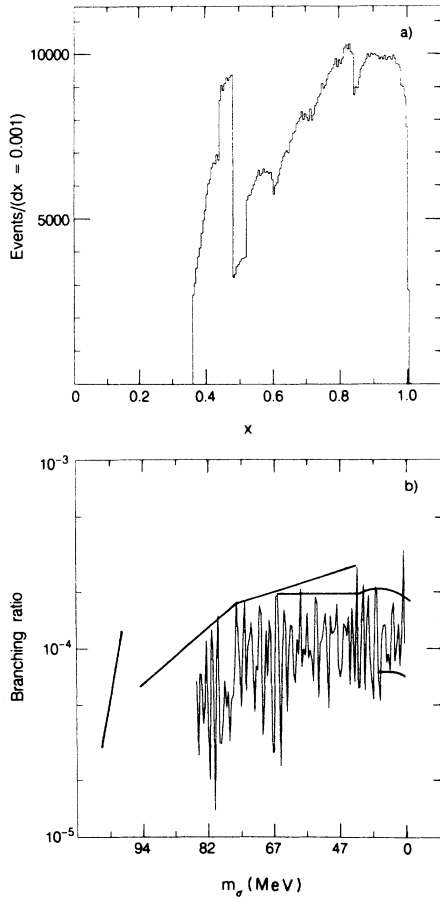

FIG. 23. Limits on the scalar decay $\mu \rightarrow e\sigma$. (a) The number of muon decay events in intervals $\Delta x = 0.001$ vs the reduced positron energy x. Only every fifth bin is plotted. This spectrum was searched for peaks indicating the decay $\mu \rightarrow e\sigma$. The spectrum represents the superposition of data from all six spectrometer settings, and the discontinuities reflect the edges of the calibrated energy range at different values of the spectrometer central field. (b) 90% C.L. on the branching ratio for the decay $\mu \rightarrow e\sigma$ vs the mass of the σ particle. As in (a), every fifth bin is plotted. The forbidden region lies above the curves. The heavy, smooth curves give an impression of the limits obtained in Ref. 37 using a similar analysis of earlier data.

times $\tau_\sigma > 10^{-8}$ sec (for $\tau_\sigma < 10^{-8}$ sec, any charged daughters from the decay of the σ would register in the μ-arm chambers, vetoing the event).

Since to first order we were concerned only with establishing the existence or absence of a peak, cuts that protected against suppression of the μSR signal could be relaxed. The decay signal was tripled by eliminating the cosine cuts of Sec. IV B and the "extra before" cuts of Sec. IV A, and by integrating the data over the full time range of the signal (Sec. VI A). Using the time distribution of the spin-held data (Fig. 17) to estimate the efficiency versus decay time of the trigger, the residual polarization of the final muon decay sample was calculated to be 3% opposite to the beam direction. Our limits therefore require a (very small) model-dependent adjustment depending on the chirality of the leptonic current.

The final sample for this analysis was binned in steps of 0.001 in x over the range $0.36 < x < 1.00$. Since the shape of the spectrum was acceptance dominated [Fig. 23(a); the discontinuities are due to acceptance cutoffs at different Φ_s settings], a quadratic fit to the continuum was made using bins to either side of an eleven-bin range centered on the position of a possible scalar peak. Near the cutoffs in the spectrometer acceptance, more poorly calibrated data (not shown) just outside the cutoff were also included in the background fit. After subtracting the continuum contribution, we used the five bins centered on the eleven-bin range to limit the height of a possible peak. Statistical errors in the background fit were included. This procedure was repeated for ranges centered on each x bin between 0.36 and 0.995.

In obtaining these limits, the line shape was fixed as a Gaussian with $\sigma_x = 0.002$. This represents a crude but fair estimate of the energy resolution, taking into account the uncertainties in the corrections to y_r in the absolute calibration as well as the spectrometer resolution given in Table III. We verified that the results were not sensitive to the precise value of σ_x.

After normalizing the fit results by the total muon decay rate, we obtained the 90%-confidence-level (C.L.) branching-ratio limits shown in Fig. 23(b). For clarity, limits only for every fifth bin have been plotted. For comparison, the limits obtained by Bryman and Clifford[37] on the basis of earlier data, including data taken with this apparatus,[3] are indicated by smooth lines. The limits reported here are more than a factor of 2 stronger across most of the spectrum. We also note that for isotropic decays with $m_\sigma = 0$, our previous end-point rate measurements[3] imply a 90%-C.L. limit of 2.6×10^{-6} on this branching ratio.

IX. CONCLUSION

We have made precise measurements of the muon decay asymmetry as a function of the positron energy. The main result is a new determination of the muon-decay parameter $\delta = 0.7486 \pm 0.0026(\text{stat}) \pm 0.0028(\text{sys})$. We have also set limits on the parameters in certain L-R-symmetric and supersymmetric extensions of the standard model. Lastly, we have used the measured muon decay spectrum to set limits on the lepton-

number-violating decay $\mu \to e\sigma$.

When considering an improved version of this experiment, it should be kept in mind that the mass scales probed for alternative physics (< 300 GeV/c^2) may be directly accessible in the near future at the Fermilab collider.[38] At lower energies, measurements of semileptonic weak processes[39] can be more sensitive than the δ parameter to universal (rather than purely leptonic) breakdowns of the standard model. However, it follows from just these observations that a measurement of δ significantly different from the value of $\frac{3}{4}$ predicted by the standard model would be all the more exciting. Whatever the source, any physics beyond the standard model would be worth the greatest effort in its discovery.

APPENDIX A: ENERGY LOSS AND STRAGGLING

The most demanding aspect of the experimental analysis was to accurately model the interactions of positrons with the 240–270-mg/cm^2 of material downstream of the muon decay point. The results were needed in the Monte Carlo simulation and in fitting measured positron spectra (such as the decay edges of Sec. V A and the straight-through distributions of Sec. V B 3) with theoretical distributions. The important phenomena were Bhabha scattering and bremsstrahlung. Both diverge as the energy loss $\epsilon = x_i - x_f$ goes to zero:

$$d\sigma_e/d\epsilon \propto 1/\epsilon^2, \quad d\sigma_\gamma/d\epsilon \propto 1/\epsilon .$$

These divergences are cut off by atomic binding effects, but simplify modeling of the energy loss by dividing the energy-loss spectrum into two parts.[8,40] The most *probable energy loss* Δ_{MP} accounts for the effects of the "divergent" part of the spectrum. These "low-energy" interactions occur in large enough number that they can be treated by ensemble variables. The *straggling curve* $f(\chi) = f(x' - \Delta_{MP})$, which peaks at $x' = \Delta_{MP}$ (here x' is the final energy after *all* straggling events have occurred), has two components: a nearly Gaussian peak which describes fluctuations around Δ_{MP}, and a tail for the low-probability "catastrophic" scatters.

The cutoff ϵ_{min} between "low-energy" and "catastrophic" scatters depends on the experimental situation, and in particular on the accuracy of the event reconstruction. ϵ_{min} should be small compared to the total resolution σ_t, which combines the Gaussian widths of the straggling curve and the spectrometer resolution. For this experiment, the minimum of σ_t was 0.0009 at

$x = 1.00$. The cutoff was made at $\epsilon_{min} = 0.0001$. Unfortunately, for the algorithm we used to calculate the straggling curve, events with these values of ϵ still made a significant contribution to the most probable energy loss, and the calculations of Δ_{MP} and $f(\chi)$ could not in fact be completely decoupled. Small adjustments to the calculated Δ_{MP} corrected for this coupling.

1. Straggling curve

In this section we discuss the modeling of straggling events with energy loss $\epsilon > 0.0001$ to determine the straggling curve $f(\chi)$.

For Bhabha scattering, since the materials of the apparatus were light, the K-shell cutoff[40] was small compared to ϵ_{min} ($K \approx 163$ eV $= 3 \times 10^{-6}$ in x for aluminum,[19] the heaviest element in our apparatus). Atomic binding effects were therefore negligible, and the plane-wave approximation of the Bhabha-scattering theory was accurate [cf. Ref. 8, Eq. (B1); the energy distribution for Bhabha scattering has been substituted for the corresponding Moller-scattering expression]:

$$\frac{dI_e}{d\epsilon} = \frac{a}{\epsilon^2}(1 - 2s + 3s^2 - 2s^3 + s^4) . \tag{A1}$$

$dI_e/d\epsilon$ is the scattering probability per g/cm^2 in a material, and $s = x_f/x_i$. The coefficient a scales as Z/A, the atomic number over the atomic mass. For straggling in the aluminum stopping target, the formula was further modified to account for the suppression of Bhabha events by the cuts on multiple hits in $P3$ (Sec. IV B; the other multiple track cuts had little additional effect in suppressing straggling events).

For the range of momentum transfers to which we were sensitive, the screening of the nucleus by the electron cloud had to be included when modeling bremsstrahlung interactions (Ref. 9, Formula 3CS):

$$\frac{d\sigma_\gamma}{d\epsilon} \propto \frac{1}{\epsilon}[s + \tfrac{3}{4}(1-s)^2]\left[\frac{\phi(v)}{4} - \tfrac{1}{3}\ln Z - f(Z)\right] ,$$

$$f(Z) = 1.2021(Z/137)^2 ,$$

$$\phi(v) = 20.4 - 4v/3, \quad v = 0.97\epsilon/x_i x_f .$$

$\phi(v)$ is the average of ϕ_1 and ϕ_2 plotted in Fig. 1 on p. 927 of Ref. 9. The term in square brackets is the uncorrected bremsstrahlung phase space; the term in large parentheses gives the screening and Coulomb wavefunction corrections. This was used to correct Tsai's formula [Ref. 8, Eq. (B2)]:

$$\frac{dI_\gamma}{d\epsilon} = \frac{1}{t_0}\frac{b}{\epsilon}[s + \tfrac{3}{4}(1-s)^2]\left[\frac{\phi(v)}{4} - \tfrac{1}{3}\ln Z - f(Z)\right] ,$$

$$b = \frac{4}{3}\left[1 + \frac{1}{9}\frac{(Z+1)/(Z+\eta)}{\ln(183Z^{-1/3})}\right] , \tag{A2}$$

$$\eta = \frac{\ln(1440Z^{-2/3})}{\ln(183Z^{-1/3})} .$$

t_0 is the radiation length in g/cm^2, so this is the bremsstrahlung probability per g/cm^2.

The straggling curve was calculated in several steps. First, the interaction probability $I(x_i, Z, A)$ for unit thickness of a given element was calculated by integrating Eqs. (A1) and (A2) for $\epsilon > 0.0005$. Since the total interaction probability was 90%, the apparatus was divided into segments $d(\rho l)$ for which $Id(\rho l) < 10\%$ to allow simulation of events with more than one catastrophic interaction. The positron spectrum was then straggled by the distribution of Eq. (A1) or Eq. (A2) according to the probabilities $I_e d(\rho l)$ and $I_\gamma d(\rho l)$. In the Monte Carlo simulation a random-number generator was used to determine whether and how much energy was lost. In fitting the data spectra, the initial positron energy distribution was simply convoluted with the energy-loss distributions.

To save computational effort, straggling with ϵ between 0.0001 and 0.0005 was simulated separately. The energy loss was subdivided in small probability steps and the straggling spectra were approximated by $dI_e/d\epsilon \propto 1/\epsilon^2$, $dI_\gamma/d\epsilon \propto 1/\epsilon$. After accumulating the effects of all the material in the apparatus, the resulting spectrum was normalized to unity. Then, as appropriate to the application, the final distribution was either sampled randomly or used in a convolution to obtain the final positron distribution.

Lastly, the Gaussian spreading of the peak was included when fitting the data by smearing, and in the Monte Carlo simulation by including events down to $\epsilon = 0.00001$ in the calculation described in the paragraph above.

2. Most probable energy loss

Δ_{MP} has been calculated for positrons by Rohrlich and Carlson:[41]

$$\Delta_{MP} = \zeta T \left[\ln \frac{\zeta T^2 2(\gamma + 1)}{K^2} - \beta^2 + 0.37 - 2.8 C \zeta \right],$$

$$\zeta = \frac{2\pi e^4}{mc^2 \beta^2} N_A \frac{d(\rho l)}{T} \frac{Z}{A}, \quad C = \beta^2 [2 - (\gamma + 1)^{-2}].$$

T is the electron kinetic energy, K is again the K-shell cutoff in the Landau theory, and β and γ are the standard relativity parameters. Unfortunately this expression does not include higher-order corrections to the energy loss, such as the "density effect" (polarization of the ionization medium[19]). To account for these effects, which can be substantial, we compared the theoretical expressions for Δ_{MP} and the mean energy loss $D_m = dE/d(\rho l)$ given in Ref. 41. For relativistic positrons:

$$\frac{\Delta_{MP} - D_m}{D_m} = \frac{1.37 + \ln \zeta}{\ln[2T^2(\gamma + 1)/I^2] - 2}.$$

The material-dependent parameters, buried in the logarithms, were relatively constant in our case. For 250 mg/cm^2 of material, $\Delta_{MP} \approx 0.8 D_m$. Taking D_m from the energy loss tables of Ref. 19, which include the higher-order corrections to the energy loss, we obtained a similarly corrected value of Δ_{MP}, accurate to better than 4%.

A different approach was used to generate the correct energy loss in the Monte Carlo simulation. The tabulat-

ed D_m was applied at each segment $d(\rho l)$ in the straggling simulation, and then decreased by the average energy loss in the applied straggling curve. The two methods were compared by generating simulated events with $x_i = 1.00$, 0.86, 0.72, 0.60, 0.50, and 0.42. The final peak positions agreed with the calculated values to within 0.0003 in x.

Before applying the calculated Δ_{MP} to the data, two further refinements were needed. First, not all the most probable energy loss was taken out of the straggling algorithm, and the peak of the curve $f(X)$ shifted as a result of compounding the $1/\epsilon$ and $1/\epsilon^2$ spectra. This shift amounted to 0.0004 in x, independent of the initial energy. Second, because of their finite width, the peaks of the Gaussian positron momentum distributions in the calibration data did not shift by exactly $\Delta x = \Delta_{MP}/E_e(\max)$. The precise shift depending on which of the peak positions algorithms were used [y(ave) or y(fit), Appendix B]. With $\Delta_{MP} = 0.0093$ for beam positrons, the calculated corrections were $+0.0011$ for y(ave), and $+0.0006$ for y(fit).

APPENDIX B: ABSOLUTE CALIBRATION: DATA REDUCTION AND FIT

In this appendix we describe in detail the collection and analysis of the beam positron data used for the absolute calibration of the spectrometer.

1. Calibration data

Two calibration runs were performed, one early and one late in the experiment. Data were collected as follows. The spectrometer and solenoid were powered in one of the six data-taking configurations ($\Phi_s = 0.42$, 0.50, 0.60, 0.72, 0.86, and 1.00). In the earlier calibration, the beam line was then tuned at each of five settings: $\Phi_b/\Phi_s = 1.18$, 1.09, 1.00, 0.92, and 0.84. In the later calibration the format was changed to allow direct comparison with the edge scan data (Sec. V A), taken immediately before. At $\Phi_s = 1.00$, 0.72, 0.60, and 0.42, only three points at $\Phi_b/\Phi_s = 1.09$, 1.00, and 0.92 were taken. At $\Phi_s = 0.86$ and 0.50, nine points were taken at $\Phi_b/\Phi_s = 1.17$, 1.13, 1.09, 1.05, 1.00, 0.95, 0.92, 0.88, and 0.85.

To stabilize hysteresis effects, all magnets were saturated at maximum field strength before being reset to their operating values, although $B1$ and $B2$ thereby induced a dipole component in $Q2$ and $Q6$. After setting $B1$, the field strengths in the other magnets were found by scaling the values at the π-μ calibration point, except for $B2$, which required adjustments of typically 0.05% of the $\Phi_s = 1.00$ setting to center the positron spot on $F3$. 30000 straight-through triggers were taken at each setting. The analysis proceeded as for muon decays, with the standard aperture cuts and momentum reconstruction (Sec. IV). The phase space (u, v, u', v') of positrons arriving at the target was not entirely stable, and because of the momentum correlations with these coordinates (Fig. 8) further cuts were made on the fringes of the phase space to minimize fluctuations in the beam

momentum distribution. The cuts on the vertical slope v' also increased the similarity between the positron momentum distribution and the muon distribution at the π-μ edge: the high-momentum fringe at large v'^2 would not have been filled by the π-μ θ function.

Correlating the reconstructed momentum distribution with the beam-line setting Y_b required much care. First, measures of the reconstructed peak position (Fig. 7) which were insensitive to the straggling tails were calculated. One measure [y_r(ave)] took consecutive averages over a decreasing range, and was sensitive to the distribution of events within the peak. Another measure [y_r(fit)] fit a parabola to the distribution of events within $\Delta y_r/y_r = 0.4\%$ of the peak center, and was primarily sensitive to the edges of the peak. Second, corrections were needed for the absolute shift Δx_b of the peak from the beam-line setting Y_b due to energy loss and straggling before measurement in the spectrometer. Assuming a Gaussian beam-line momentum acceptance, these were $\Delta x_b = 0.0104$ when using y(fit) (the parabolic peak measure applied to the true momentum distribution) and 0.0099 when using y(ave) (Appendix A 1). The assumption was checked by fitting straggled Gaussians to the data distributions, and calculating y(ave) and y(fit) for both the simulated and the actual data. The differences were usually less than 0.0001 in y(ave) and 0.0003 in y(fit), which are negligible. Figure 7 shows a sample fit in the extreme: the discrepancy in y(fit) is 0.0003.

In spite of the differences outlined above, the calibration fit results were independent of the peak measure chosen.

2. Calibration fit

We describe here the fit to the combined calibration data: the μ-e and π-μ reference points of Sec. V B and the beam positron data described above. The fit determined the beam-line and spectrometer calibration curves Eqs. (5.1) and (5.2) and the final corrections to the relative momentum y_r obtained after applying the results of Sec. V A. Using the π-μ and μ-e benchmarks, m_b and

m_s were eliminated from Eqs. (5.1) and (5.2) ($Y_{\pi\mu} = 0.5639$, $Y_{\mu e} = 1.0000$):

$$Y_b(B_1, B_{1,0}) = Y_{\pi\mu} \frac{B_1 - B_{1,0}}{B_{1,\pi\mu} - B_{1,0}} \ ,$$

$$Y_s(B_s, B_{s,0}) = Y_{\mu e} \frac{B_s - B_{s,0}}{B_{s,\mu e} - B_{s,0}} \ .$$

As discussed in Sec. V B, the two inconsistent measurements of $B_{1,\pi\mu}$ required distinct calibration fits, while the spectrometer μ-e measurement $B_{s,\mu e} = 3186.7$ G was highly reproducible. The corrections to the relative momentum were taken to be second order in y_r and constrained to be zero at $y_r = 0.9917$. The transformation which converted y_r to the initial positron momentum y was therefore of the form

$$y - \Delta x = Y_s[y_r + a(y_r - 0.9917) + b(y_r - 0.9917)^2] \ .$$

$$\text{(B1)}$$

Δx is the energy loss experienced by the positron before reaching the spectrometer. a and b, the linear and quadratic coefficients of the corrections to y_r, were allowed to vary linearly with Y_s:

$$a = a_0 + a_1(1 - Y_s), \quad b = b_0 + b_1(1 - Y_s) \ .$$

The free parameters to be determined in the calibration fit were therefore $B_{1,0}$, $B_{s,0}$, a_0, a_1, b_0, and b_1.

Each of the 30 calibration points (29 in the later data set) contributed three pieces of information to the fit (i indexes the data point): B_1^i (or B_2^i), y_r(ave)^i [or y_r(fit)^i], and B_s^i. With the energy loss experienced by the beam positrons in traversing the apparatus to reach the spectrometer calculated to be $\Delta x_b = 0.0104$ [or 0.0099 for y_r(fit)], we made the identifications in Eq. (B1):

$$y = Y_b(B_1^i, B_{1,0}), \quad Y_s = Y_s(B_s^i, B_{s,0}) \ ,$$

$$y_r = y_r^i(\text{fit}) \ .$$

The relative calibration data of Table III were also in-

TABLE X. Momentum calibration results. The fit results to the early and late calibration data of Sec. V and Fig. 16, with the spectrometer zero-point $B_{s,0}$ indicated by the bending magnet B_1 or B_2 used to calibrate the beam line. The fit errors on the parameters were small compared to the early-late differences. The fit values of a and b were essentially unchanged after the switch from B_1 to B_2.

| | Data and $\pi\mu$ calibration set | |
	Earlier	Later
a	$(-1.2 - 0.6Y_s) \times 10^{-3}$	$(-2.5 - 16.3Y_s) \times 10^{-3}$
b	$-0.048 - 0.001Y_s$	$-0.013 - 0.042Y_s$
B_1 beam-line calibration		
$B_{s,0}$	16.6 G	8.4 G
$B_{1,0}$	2.7 G	-1.7 G
$B_{1,\pi\mu}$	875.6 G	874.8 G
χ^2/DF	38/33	31/33
B_2 beam-line calibration		
$B_{s,0}$	13.3 G	3.4 G
$B_{2,0}$	0.4 G	-3.4 G
$B_{2,\pi\mu}$	954.3 G	952.6 G
χ^2/DF	30/33	39/33

cluded in the fit, contributing nine points (indexed by j):

$$y - \Delta x_s = 0.9917, \quad Y_s = Y_s(B_s^j, B_{s,0}), \quad y_r = y_{r,\mu e}^j .$$

These helped to stabilize the corrections to y_r in the later calibration data, which were very sensitive to fluctuations in the points at $\Phi_s = 1.00$ and 0.42.

The results of a χ^2 fit to these data are exhibited in Table X for both the early and late sets of calibration data. The change in $B_{s,0}$ when calibrating the beam line with B_2 rather than B_1 is also given (the corrections to y_r were unaffected). With a systematic error $\sigma_Y = 0.0005$ assigned to the data points, we obtained a $\chi^2/\mathrm{DF} \approx 1$ [note that the residuals in Figs. 16(e) and 16(f) must be scaled by the spectrometer setting before being compared to this uncertainty]. However, this measure of the calibration accuracy is misleading. As seen in Fig. 16 and discussed in Sec. V B 3, the two calibrations showed differences which were sometimes as large as 0.0015 in the conversion of Eq. (B1). Correspondingly, the differences between the parameters fit using the early and late data were all much larger than the fit one-standard-deviation errors. It was therefore our inability to reproduce the calibration conditions, rather than the fundamental limitations of the beam-line design, which limited the precision of the calibration.

APPENDIX C: π-μ CALIBRATION SHIFT

As discussed in Sec. VII B 1 the shift in the beam-line π-μ calibration point between the early and later calibration runs was an important contributor to one of the larger errors in the determination of δ. Here we complete the description of the analysis of the π-μ calibration points begun in Sec. V B 1, and then consider explanations for the shift. Three effects were expected to be accounted for by a successful explanation: the shift in the π-μ point; the differences in the relative shifts in $B_{1,\pi\mu}$ and $B_{2,\pi\mu}$ (0.09% vs 0.17%); and the shift in the spectrometer zero point. A beam-line hysteresis hypothesis satisfied all three criteria, but did not enable an unambiguous selection of one measurement over the other. Thus, the two measurements were accepted with equal weight in the analysis.

The data for the two calibrations (Fig. 15) were fit to the form

$$F = \frac{(\mu \text{ STOP})}{(\text{BEAM})} = \frac{NI + F_0}{1 + NI} . \tag{C1}$$

F_0 is the pedestal signal above the $\pi\mu$ edge where the muon flux is dominated by pion decay in flight at 1AT1, $I = I(B_{1-}B_{1,\pi\mu}, \sigma_b)$ is the overlap of the Gaussian beam-line acceptance and the θ-function momentum distribution for surface muons arising from pion decay at rest at 1AT1, σ_b is the Gaussian width in Y_b of the beam-line acceptance; and N is a flux factor for the surface muons. F_0, N, $B_{1,\pi\mu}$, and σ_b were determined in a χ^2 fit to the data of Fig. 15. As discussed in Sec. V B 1, the two data sets gave significantly different results: for the earlier calibration $B_{1,\pi\mu} = 875.6$ G and $B_{2,\pi\mu} = 954.3$ G. While for the later $B_{1,\pi\mu} = 874.8$ G and

$B_{2,\pi\mu} = 952.6$ G. The statistical uncertainty in the fit values was 0.2 G.

We now carefully consider Fig. 15. Since muons accounted for less than 2% of the beam flux above the π-μ edge (Fig. 5), the pedestal must have been due primarily to spurious μ-stop signals resulting from inefficiencies for positrons in the downstream chambers (Sec. V B 1). Clearly, the dramatic increase in the threshold seen in the later calibration required a dramatic change in the experimental conditions. The increase in the proton current on 1AT1 from 30 (earlier calibration) to 130 μA (main data taking and later calibration), and a corresponding fourfold increase in the beam-line flux, stands out. We hypothesize that the downstream chambers began to saturate (i.e., become unresponsive to positron hits) at the higher flux. Since the loss in efficiency indicated was large (40%), it might seem reasonable to reject the second measurement altogether. However, that would leave us without a check on the π-μ calibration. Furthermore, inefficiency in the downstream chambers should only change the pedestal F_0 in Eq. (C1). Saturation could produce a change in $B_{1,\pi\mu}$ only in complicated scenarios in which the upstream chambers were also inefficient for positrons, and that inefficiency was dependent on the muon flux. The rejection of straight-through positrons seen in Fig. 12, indicating high efficiency in the upstream chambers, ruled out such possibilities.

Second, we considered the potential effects of hysteresis in the beam-line bending magnets. The calibration procedure (Appendix B) called for saturation of $B1$ and $B2$ at maximum current each time the central fields were changed, although dipole fields were thereby induced in $Q2$ and $Q6$. The complicating factor was that the strength of the induced dipole component in $Q2$, for example, depended on whether its current was set before or after $B1$ was saturated. Unfortunately, no particular procedure was adopted to ensure consistency in the data as concerns this point. In studies done after the experiment, the two cases were observed to give a 0.14% difference in $B_{1,\pi\mu}$. This agrees well with the differences seen between the two π-μ measurements: 0.09% in $B_{1,\pi\mu}$ and 0.17% in $B_{2,\pi\mu}$.

Long-term magnet and power supply instabilities were also investigated, in this case using the measured positron end points in the $\Phi_s = 1.00$ data and the beam positron peaks in the $\Phi_s = 0.50$ and 0.60 data. Both the beam line and spectrometer were found to be very stable. As already noted (Sec. V B 2), the end point in the spin-precessed data varied by only ±0.0002 over the course of the experiment. Similarly, analysis of the straight-through positron peak (Fig. 12, Appendix B) showed y(ave) = 0.5508(3) for the $\Phi_s = 0.50$ runs and y(ave) = 0.5504(2) for the $\Phi_s = 0.60$ runs. Only one significant difference was seen, when the data were divided into samples taken before and after the later calibration. The 20 earlier runs had y(ave) on average 0.0003 higher than the later eight (the earlier calibration fit results were used in analyzing both samples). Since the cyclotron was retuned following maintenance just before the later calibration, such a shift was not surprising:

slight changes in the proton spot at 1AT1 and thus in the beam-line momentum bite were to be expected (see below). However, the difference is not significant compared to the 0.0011 difference in the two beam-line calibrations [Eq. (5.1)] at these momenta.

The observed stability of the spectrometer eliminated changes in the spectrometer field as an explanation of the early-late difference in $B_{s,0}$. Other effects could only cause the shift by introducing an error into the beam-line calibration curve. The beam-line hysteresis effect described above is a good example. In that case, one of the calibrations is simply wrong. When it is used to calculate the momentum of beam positrons, the systematically incorrect results yield an apparent shift in $B_{s,0}$. Conversely, motion of the proton spot on 1AT1 cannot explain the change in $B_{s,0}$. Changes of less than 1 mm were allowed by the monitoring equipment (Sec. III A), and might have been expected when the proton current was increased from 30 to 130 μA or following cyclotron retuning. Any systematic horizontal motion would have been reflected in the source distribution seen by M13, and would have appeared as a shift of up to 0.0005 in Y_b at the π-μ calibration point. This effect could not explain the change in $B_{s,0}$, though, since the motion of the proton spot would have had the same effect on the muon and positron sources. Although the calibration curve

[Eq. (5.1)] might have changed, it would still yield correct results for the transmitted positron momentum.

In conclusion, though many effects were clearly involved in creating differences between the two π-μ calibration measurements, it seemed likely that hysteresis in the beam-line magnets was primarily responsible for the corresponding changes in the spectrometer calibration results, and in particular for the change in $B_{s,0}$. Unfortunately, it is not possible under this hypothesis to choose one of the calibration points over the other. That the individual π-μ calibration points and data sets could not be correlated was checked by fitting both beam positron data sets using the first π-μ measurement. After accounting for the 0.0003 shift in the beam-line setting following cyclotron retuning, the difference in the spectrometer calibration curve [Eq. (5.2)] was only 0.0004 in y at $\Phi_s = 0.50$ (in comparison, the systematic error on the data points was 0.0005 in y and the π-μ calibration discrepancy corresponded to a difference at $\Phi_s = 0.50$ of 0.0013 in y). Fitting both data sets independently with the second calibration point also gave consistent results. All possible combinations of the π-μ measurements and beam positron data sets were therefore considered with equal weight in evaluating systematic errors on the decay parameters in Sec. VII.

---

*Present address: Lawrence Livermore National Laboratory, L-421, P.O. Box 808, Livermore, CA 94550.

†Present address: Bell Communications Research, 331 Newman Springs Rd., Red Bank, NJ 07701-7020.

‡Deceased.

§Present address: Department of Physics, The Johns Hopkins University, Baltimore, MD 21218.

**Present address: Department of Physics, University of Colorado, Boulder, CO 80309.

[1]S. Glashow, Nucl. Phys. **22**, 529 (1961); S. Weinberg, Phys. Rev. Lett. **19**, 1264 (1967); A. Salam, in *Elementary Particle Theory: Relativistic Groups and Analyticity (Nobel Symposium No. 8)*, edited by N. Svartholm (Almqvist & Wiksell, Stockholm, 1968).

[2]F. Scheck, Phys. Lett. C **44**, 187 (1978).

[3]A. Jodidio *et al.*, Phys. Rev. D **34**, 1967 (1986); D. P. Stoker *et al.*, Phys. Rev. Lett. **54**, 1887 (1985); J. Carr *et al.*, *ibid.* **51**, 627 (1983).

[4]D. Fryberger, Phys. Rev. **166**, 1379 (1968).

[5]We ignore finite W_L mass effects. This implies (negligible) corrections of $O(m_\mu^2/m_W^2)$.

[6]Particle Data Group, C. G. Wohl *et al.*, Phys. Lett. **170B** (1986). Primary input to ρ is from J. Peoples, Nevis Cyclotron Report No. 147, 1966 (unpublished); primary input to η is from F. Corriveau *et al.*, Phys. Lett. **129B**, 260 (1983); S. E. Derenzo, Phys. Rev. **181**, 1854 (1969); primary input to ξP_μ is from V. V. Akhmanov *et al.*, Yad. Fiz. **6**, 316 (1966) [Sov. J. Nucl. Phys. **6**, 230 (1967)]; primary input to δ is from Ref. 4; primary input to $\xi P_\mu \delta / \rho$ is Ref. 3.

[7]A. M. Sachs and A. Sirlin, in *Muon Physics*, edited by V. Hughes and C. S. Wu (Academic, New York, 1975), Vol. III, p. 50. In this discussion of the internal radiative corrections, standard-model values of the decay parameters are as-

sumed. This was sufficient for our analysis. For calculations in the general case, see V. Flourescu and O. Kamei, Nuovo Cimento **61A**, 967 (1968).

[8]Y. S. Tsai, Stanford Linear Accelerator Report No. SLAC-PUB-848, 1971 (unpublished), Appendix B.

[9]H. W. Koch and J. W. Motz, Rev. Mod. Phys. **31**, 920 (1959).

[10]C. J. Oram, J. B. Warren, G. M. Marshall, and J. Doornbos, Nucl. Instrum. Methods **179**, 95 (1981).

[11]D. A. Ross, Nuovo Cimento **10A**, 475 (1972); A. V. Kuznetsov and N. V. Mikheev, Yad. Fiz. **30**, 258 (1979) [Sov. J. Nucl. Phys. **30**, 131 (1979)].

[12]For magnet monitoring, we used NMR probes developed by R. Openshaw at TRIUMF (three different models were needed to cover the range from 600 to 4200 G), and commercial Hall probes by F. W. Bell [models BH-701 (high sensitivity, linear to 0.1%), BH-702 (concentrator), and BH-705].

[13]D. P. Stoker, Ph.D. thesis, Lawrence Berkeley Laboratory Report No. LBL-20324, 1985.

[14]W. P. Trower, Lawrence Radiation Laboratory Report No. UCRL-2426, 1966 (unpublished).

[15]R. M. Sternheimer, Phys. Rev. **117**, 485 (1960).

[16]K. Halbach (private communication). In the first-order optics approximation, the radial component of the field off axis is estimated from the gradient of the longitudinal field on axis. See Appendix A of Ref. 13 for details.

[17]F. James and M. Roos, CERN Computer Center Reports Nos. D506 and D516 (unpublished).

[18]R. Kubo and K. Tomita, J. Phys. Soc. Jpn. **9**, 888 (1954).

[19]M. J. Berger and S. M. Seltzer, U.S. National Bureau of Standards Report No. NBSIR 82-2550-A, 1982 (2nd ed.) (unpublished).

[20]G. W. Ford and C. J. Mullin, Phys. Rev. **108**, 477 (1957).

[21]We thank Professor H.-J. Gerber for alerting us to the error in Ref. 20.

[22]K. W. Kehr *et al.*, Z. Phys. B **32**, 49 (1978).

[23]D. Richter, in *Neutron Scattering and Muon Spin Rotation* (Springer Tracts in Modern Physics 101) (Springer, Berlin, 1983), p. 85.

[24]K. Mursula and F. Scheck, Nucl. Phys. **B253**, 189 (1985).

[25]H. Burkard *et al.*, Phys. Lett. **160B**, 343 (1985).

[26]W. Fetscher, H.-J. Gerber, and K. F. Johnson, Phys. Lett. B **173**, 102 (1986).

[27]D. P. Stoker, in *Intersections Between Particle and Nuclear Physics*, Lake Louise, Canada, 1986, edited by Donald F. Geesaman (AIP Conf. Proc. No. 150) (AIP, New York, 1986), p. 976.

[28]B. Balke *et al.*, in *Proceedings of the 22nd International Conference on High Energy Physics*, Leipzig, East Germany, 1984, edited by A. Meyer and E. Wieczorek (Akademie der Wissenschaften, Zeuthen, 1984), Vol. 1, p. 208.

[29]J. C. Pati and A. Salam, Phys. Rev. D **10**, 275 (1974); R. N. Mohapatra and J. C. Pati, *ibid.* **11**, 566 (1974); **11**, 2558 (1974); G. Senjanović and R. N. Mohapatra, *ibid.* **12**, 1502 (1975); G. Senjanović, Nucl. Phys. **B135**, 334 (1979).

[30]H. P. Nilles, Phys. Rep. **110**, 1 (1984).

[31]As concerns supersymmetry, see H. Haber and G. Kane, Phys. Rep. **117**, 75 (1985); S. Dawson, Nucl. Phys. **B261**, 297 (1985).

[32]K. Mursula, M. Roos, and F. Scheck, Nucl. Phys. **B219**, 321 (1983); K. Mursula *ibid.* **B241**, 173 (1984).

[33]W. Buchmüller and F. Scheck, Phys. Lett. **145B**, 421 (1984).

[34]C. Hearty *et al.*, Phys. Rev. Lett. **58**, 1711 (1987); C. Hearty (private communication).

[35]R. E. Shrock, Phys. Rev. D **24**, 1275 (1981).

[36]D. Reiss, Phys. Lett. **115B**, 217 (1982); F. Wilczek, Phys. Rev. Lett. **49**, 1549 (1982).

[37]D. A. Bryman and E. T. H. Clifford, Phys. Rev. Lett. **57**, 2787 (1986).

[38]E. Eichten, in *High Energy Physics 1985*, proceedings of the Theoretical Advanced Institute in Elementary Particle Physics, New Haven, Connecticut, 1985, edited by J. Bowick and F. Gursey (World Scientific, Singapore, 1985), p. 709.

[39]A. I. Boothroyd, J. Markey, and P. Vogel, Phys. Rev. C **29**, 603 (1984).

[40]L. Landau, J. Phys. (USSR) **8**, 201 (1944).

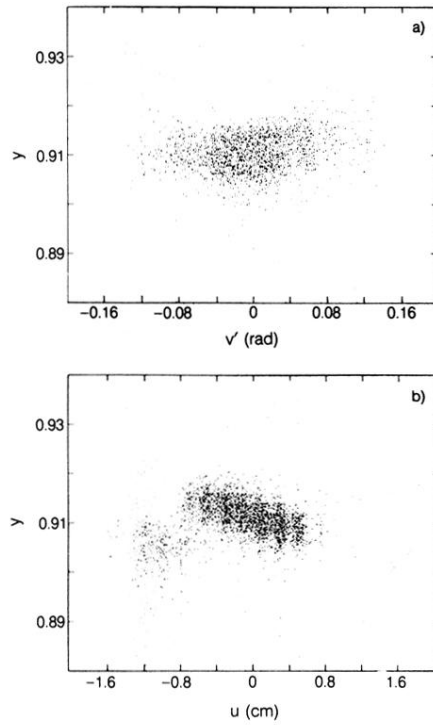[41]F. Rohrlich and B. C. Carlson, Phys. Rev. **93**, 38 (1954).

FIG. 8. Beam positron momentum correlations at *F*3. Correlations of the momentum delivered by the beam line with coordinates at the final focus *F*3, in a Cartesian system with w along the beam axis, u horizontal, v vertical, $u'=du/dw$, and $v'=dv/dw$. (a) Momentum y of beam positrons vs the vertical slope v' at *F*3. Cuts were made at $v'=\pm0.05$ rad. (b) Positron momentum vs the horizontal coordinate u at *F*3. (b) and Fig. 9 indicate the presence of unexpected material in the target area near *S*1. Cuts were made at $u=\pm0.7$ cm.